Master 2 CSMI : Scientific Computation and Mathematics of Innovation

Well-balanced semi-implicit scheme for the Euler equations with gravity

Host Organization: ITI IRMIA++

Author:
Oussama BOUHENNICHE

Supervisor:
Ms. Andrea THOMANN
Mr. Victor Michel DANSAC

August 21, 2025

Acknowledgements

This Master's internship has been an enriching and formative experience that would not have been possible without the support, guidance, and encouragement of many people.

I would like to sincerely thank my supervisors, Andrea Thomann and Victor Michel-Dansac at Inria, for their guidance, availability, and valuable feedback throughout this internship. Their expertise, insightful advice have been instrumental in shaping this work. I am deeply grateful for their patience and for the time they dedicated to follow my work closely.

On a more personal note, I would like to dedicate this work to the memory of my beloved mother, whose strength and love continue to inspire me every day. I also want to express my deepest gratitude to my sisters, Sihem, Soumia, and Asma, for their unwavering support, encouragement, and affection throughout this journey. Their presence has been a constant source of motivation and resilience.

Finally, I would like to thank all those who, directly or indirectly, contributed to making this experience a valuable and memorable step in my academic journey.

Abstract : We propose a well-balanced semi-implicit scheme for the compressible Euler equations with gravity, designed to overcome the acoustic CFL restriction and to preserve hydrostatic equilibria. The method combines asymptotic-preserving and well-balanced properties through a flux-splitting strategy with implicit pressure–gravity coupling and explicit transport discretization with second-order extension. Numerical tests, including equilibrium preservation and instabilities such as Rayleigh–Taylor and rising bubble problems, demonstrate the efficiency and reliability of the approach across different flow regimes.
keywords : Euler equation, well-balanced numerical scheme, asymptotic-preserving

Contents

1 Introduction

The compressible Euler equations with gravitational source terms play a central role in the mathematical modeling of many natural phenomena. They arise in a wide range of applications, from geophysical flows such as atmospheric and oceanic circulation, to astrophysical dynamics including stellar structures, accretion disks, or buoyancy-driven instabilities. These flows are strongly influenced by the presence of gravity, which generates equilibria where the pressure gradient balances the gravitational force.

A particular difficulty in the numerical simulation of such systems lies in the fact that many of these flows evolve in low-Mach-number regimes, where the flow velocity is much smaller than the speed of sound. In this context, explicit schemes suffer from two major drawbacks:

(i) They are subject to the acoustic CFL restriction, which forces prohibitively small time steps due to the presence of fast acoustic waves, although the physical dynamics of interest evolve on much slower time scales.

(ii) They generally fail to preserve delicate steady states, such as hydrostatic equilibria, which may result in spurious oscillations, numerical instabilities, or unphysical long-time behavior.

To address these challenges, we want to propose a numerical scheme that combines these two key properties:

1. *Asymptotic-Preserving (AP)* schemes, which are designed to remain stable and accurate in the low-Mach-number limit, effectively filtering out acoustic waves and allowing for larger time steps.

2. *Well-Balanced* schemes, which are specifically tailored to preserve hydrostatic equilibria at the discrete level, ensuring that the numerical solution remains close to these steady states even in the presence of perturbations.

Nevertheless, combining these two properties within a single numerical method, while maintaining efficiency and robustness for a broad range of regimes, remains a nontrivial task. This forms the core problem addressed in the present work.

In this internship, we propose the development of a well-balanced semi-implicit scheme for the compressible Euler equations with gravity. The main ingredients of the approach are the following:

- Flux-splitting strategy, in which the transport (convective) terms are discretized explicitly, while the pressure gradient and gravitational source terms are handled implicitly.

- The formulation of the implicit step as a linear elliptic problem for the pressure or the total energy, depending on the chosen formulation, which ensures stability across different flow regimes.

- The use of IMEX Runge–Kutta methods to achieve high-order temporal accuracy while efficiently combining explicit and implicit contributions.

- Finite volume discretization on Cartesian grids, which guarantees robustness and makes the method suitable for both equilibrium preservation and complex dynamical simulations.

The proposed method is designed to meet three key objectives:

1. Remove the acoustic time step restriction, allowing larger time steps independent of the Mach number.

2. Preserve hydrostatic equilibria exactly through a well-balanced treatment of the fluxes and source terms.

3. Remain asymptotic-preserving in the low-Mach regime, ensuring physically consistent results without numerical instabilities.

To evaluate the performance of the scheme, we carry out an extensive set of numerical experiments. These include classical benchmarks such as equilibrium preservation and accuracy tests, as well as more challenging configurations like the Rayleigh–Taylor instability and the rising bubble problem.

This work contributes to the development of versatile framework capable of handling a variety of geophysical and astrophysical problems while maintaining a good balance between stability, accuracy, and computational cost.

This internship was conducted within the **Macaron team** (**MAC**hine le**AR**ning for **O**ptimized **N**umerical methods) at **Inria Nancy–Grand Est**, hosted in Strasbourg. The team focuses on the development of numerical methods and reduced models that combine classical approaches with modern learning techniques. This internship was funded by **ITI IRMIA++** and carried out under the supervision of **Andrea Thomann** and **Victor Michel-Dansac**.

2   The Euler equations with gravity

Euler equations are considered as a cornerstone of fluid dynamics. It describes the motion of a compressible fluid without viscosity, based on the conservation of mass, momentum, and energy. They were first derived by Leonhard Euler in 1757 [1], and since then they have served as the foundation for both theoretical studies and numerical simulations of fluid flows in a wide range of applications, including aerodynamics, astrophysics, and geophysical fluid dynamics [2, 3].

In their classical form, the Euler equations are written as:

$$\frac{\partial \rho}{\partial t} + \nabla \cdot (\rho \mathbf{u}) = 0, \tag{1a}$$

$$\frac{\partial (\rho \mathbf{u})}{\partial t} + \nabla \cdot (\rho \mathbf{u} \otimes \mathbf{u}) + \nabla p = 0, \tag{1b}$$

$$\frac{\partial \rho E}{\partial t} + \nabla \cdot (\mathbf{u}(\rho E + p)) = 0, \tag{1c}$$

Where ρ denotes the density, $\mathbf{u}$ the velocity field, p the pressure, and E the total energy defined by:

$$E = \rho e + \tfrac{1}{2}\rho\|\mathbf{u}\|^2, \tag{2}$$

.

In this work, we are interested in a rescaled form of the Euler system that incorporates the effect of a gravitational potential ϕ in d space dimensions.

In dimensional form, the governing equations are:

$$\partial_t \rho + \nabla \cdot (\rho \mathbf{u}) = 0, \tag{3a}$$

$$\partial_t(\rho \mathbf{u}) + \nabla \cdot (\rho \mathbf{u} \otimes \mathbf{u}) + \nabla p = -\rho\nabla\phi, \tag{3b}$$

$$\partial_t \rho E + \nabla \cdot \big(\mathbf{u}(\rho E + p)\big) = 0, \tag{3c}$$

Where the total energy density is given by:

$$\rho E = \rho e + \tfrac{1}{2}\rho\|\mathbf{u}\|^2 + \rho\phi \tag{4}$$

The unknowns are defined on the space-time cylinder $\Omega \times [0, T]$, with $\Omega \subset \mathbb{R}^d$:

$$\rho : \Omega \times [0, T] \to \mathbb{R}_+,$$
$$\mathbf{u} : \Omega \times [0, T] \to \mathbb{R}^d,$$
$$p : \Omega \times [0, T] \to \mathbb{R}_+,$$
$$\rho E : \Omega \times [0, T] \to \mathbb{R}.$$

The gravitational potential ϕ is assumed to be time-independent and sufficiently regular so that $\nabla\phi$ is well-defined and bounded.

$$\phi : \Omega \to \mathbb{R},$$

To derive a scaled system, we introduce Reference scales:

$$\rho_0, \quad U_0, \quad p_0, \quad L_0, \quad \phi_0,$$

Then, we define the dimensionless variables:

$$\tilde{\rho} = \frac{\rho}{\rho_0}, \quad \tilde{\mathbf{u}} = \frac{\mathbf{u}}{U_0}, \quad \tilde{p} = \frac{p}{p_0}, \quad \tilde{x} = \frac{x}{L_0}, \quad \tilde{t} = \frac{tU_0}{L_0}, \quad \tilde{\phi} = \frac{\phi}{\phi_0}.$$

The reference sound speed is defined from the equation of state (EOS) by:

$$c_0^2 := \left.\frac{\partial p}{\partial \rho}\right|_s (\rho_0, s_0),$$

And evaluated at a chosen reference state (ρ_0, s_0).

The Mach number is then:

$$M = \frac{U_0}{c_0}.$$

We choose the pressure scale:

$$p_0 = \rho_0 c_0^2,$$

Which yields the standard $1/M^2$ scaling in the momentum equation.

For the gravitational scaling, we set:

$$\frac{\phi_0}{L_0} = \frac{U_0^2}{Fr^2} \quad \Longleftrightarrow \quad Fr = \frac{U_0}{\sqrt{\phi_0/L_0}},$$

So that the gravitational force term naturally appears with $1/Fr^2$.

After substitution and simplification, and omitting tildes for readability, the non-dimensional equations read:

$$\partial_t \rho + \nabla \cdot (\rho \mathbf{u}) = 0, \tag{5a}$$

$$\partial_t (\rho \mathbf{u}) + \nabla \cdot (\rho \mathbf{u} \otimes \mathbf{u}) + \frac{1}{M^2} \nabla p = -\frac{1}{Fr^2} \rho \nabla \phi, \tag{5b}$$

$$\partial_t E + \nabla \cdot \big(\mathbf{u}(E + p) \big) = 0, \tag{5c}$$

Where the non-dimensional total energy is:

$$E = \rho e + \frac{1}{2} M^2 \rho \|\mathbf{u}\|^2 + \frac{M^2}{Fr^2} \rho \phi. \tag{6}$$

Here the first term is the internal energy, while the kinetic and potential contributions appear multiplied by M^2 and M^2/Fr^2, respectively.

The parameters M and Fr denote the Mach and Froude numbers, respectively. The Mach number measures the ratio between the fluid velocity and the speed of sound, and thus characterizes the flow regime. The Froude number measures the ratio between the fluid velocity and the characteristic velocity induced by gravity, and thus quantifies the relative importance of inertial and gravitational effects.

To close the system, we adopt an equation of state (EOS). In the present work, we focus on the ideal gas law:

$$p(\rho, e) = (\gamma - 1)\rho e, \tag{7}$$

Where γ is the adiabatic index.

2.1 Hydrostatic equilibria

A particularly important class of solutions in this context are the *hydrostatic equilibria*, defined as stationary states with vanishing velocity field $\mathbf{u} = 0$.

This equilibria is obtained from The non-dimensional Euler equations (5) by replacing $\mathbf{u} = 0$ in the equation of Momentum (5b) so:

$$\partial_t(0) + \nabla \cdot (0) + \frac{1}{M^2} \nabla p = -\frac{1}{Fr^2} \rho \nabla \phi, \tag{8}$$

Which is given:

$$\mathbf{u} = 0, \qquad \frac{\nabla p}{M^2} = -\rho \frac{\nabla \phi}{Fr^2}. \tag{9}$$

This equilibria play a central role in geophysical and astrophysical flows, as they describe the balance between pressure gradients and gravitational forces. Preserving such equilibria at the discrete level is crucial for the design of robust and accurate numerical methods.

Examples of Hydrostatic Atmospheres: Two important examples of hydrostatic atmospheres illustrate this balance. In an *isothermal atmosphere*, the density and pressure profiles decay exponentially with the gravitational potential, namely:

$$\rho^{\text{hyd}}(x,y) = \exp\left(-\tfrac{M^2}{Fr^2}\phi(x,y)\right), \qquad p^{\text{hyd}}(x,y) = \exp\left(-\tfrac{M^2}{Fr^2}\phi(x,y)\right). \tag{10}$$

Another common configuration is the *polytropic atmosphere*, in which density and pressure follow power-law profiles,

$$\rho^{\text{hyd}}(x,y) = \left(1 - \tfrac{\gamma-1}{\gamma}\tfrac{M^2}{Fr^2}\phi(x,y)\right)^{\frac{1}{\gamma-1}}, \qquad p^{\text{hyd}}(x,y) = \left(1 - \tfrac{\gamma-1}{\gamma}\tfrac{M^2}{Fr^2}\phi(x,y)\right)^{\frac{\gamma}{\gamma-1}}. \tag{11}$$

These analytic atmospheres serve as canonical benchmarks for validating numerical schemes, since they provide exact equilibrium.

2.2   Asymptotic limit

Following the asymptotic analysis in [4], the *low-Mach* regime corresponds to the limit $M \to 0$ with $M \approx Fr$, a scaling that preserves hydrostatic equilibrium. This regime is relevant for many geophysical and astrophysical flows, where pressure gradients nearly balance gravity and acoustic effects are negligible relative to material transport and buoyancy.

At leading order, the Euler system reduces to the *hydrostatic balance*:

$$\nabla p^0 = -\rho^0 \nabla \phi, \tag{12}$$

where p^0 and ρ^0 are the leading-order pressure and density obtained from a Mach-number perturbation expansion, and ϕ denotes the gravitational potential. In this limit, fast acoustic modes are absent at leading order, and the dynamics evolve on slower transport- and buoyancy-driven time scales.

From a numerical standpoint, explicit Godunov-type schemes encounter two main issues in this regime:

- CFL condition is dictated by acoustic speeds, forcing prohibitively small time steps;

- Numerical viscosity inherent to Godunov fluxes scales with the largest wave speed, overdamping the slow physical modes.

These difficulties motivate implicit treatments of the acoustic terms and flux-splitting strategies that separate fast (acoustic) contributions from slow (transport and buoyancy-driven) dynamics, enabling stable and accurate simulations across a wide range of Mach numbers.

3   The numerical scheme

The objective of this section is to present the semi-implicit well-balanced scheme developed during the internship. The scheme combines explicit and implicit treatments in order to cope with stiff pressure and gravitational terms while preserving equilibrium states and ensuring stability in the low-Mach regime. We start with the reformulation of the governing equations, then derive the time semi-discrete scheme, extend it to a fully discrete setting, and finally discuss its high-order extension.

3.1   *Well-Balanced Reformulation*

In most applications, the hydrostatic equilibrium state is known a priori. Therefore, we assume the existence of a stationary solution of (9) consisting of a time-independent hydrostatic density ρ^{hyd} and a hydrostatic pressure p^{hyd} such that:

$$\frac{\nabla p^{\text{hyd}}}{M^2} = -\rho^{\text{hyd}} \frac{\nabla \phi}{Fr^2}. \tag{13}$$

This relation yields a description of the gravitational potential in terms of the hydrostatic state:

$$\nabla \phi = -\frac{Fr^2}{M^2} \frac{\nabla p^{\text{hyd}}}{\rho^{\text{hyd}}}. \tag{14}$$

Since ρ^{hyd} and p^{hyd} satisfy a spatial differential relation, they are purely spatial functions and remain constant in time.

Plugging (14) into the Euler equations (5), we obtain the following reformulation of the Euler system with gravity:

$$\frac{\partial \rho}{\partial t} + \nabla \cdot \rho \mathbf{u} = 0, \tag{15a}$$

$$\frac{\partial \rho \mathbf{u}}{\partial t} + \nabla \cdot \rho \mathbf{u} \otimes \mathbf{u} + \frac{\nabla p}{M^2} = \frac{\rho}{\rho^{\text{hyd}}} \frac{\nabla p^{\text{hyd}}}{M^2}, \tag{15b}$$

$$\frac{\partial E}{\partial t} + \nabla \cdot (\mathbf{u}(E + p)) = 0. \tag{15c}$$

This formulation highlights the crucial point: the stiff pressure terms appear in the momentum equation and the hydrostatic source term. To handle this stiffness efficiently, we split the fluxes into two contributions:

- **explicit part**, containing convective terms,

- **implicit part**, containing the stiff pressure contributions and the gravitaionnel source.

We denote by:

$$\mathbf{q} = \begin{pmatrix} \rho \\ \rho \mathbf{u} \\ E \end{pmatrix}$$

The vector of conservative variables.
The explicit part reads:

$$\mathbf{f}(\mathbf{q})^{\mathbf{u}} = \begin{pmatrix} \rho \mathbf{u} \\ \rho \mathbf{u} \otimes \mathbf{u} \\ 0 \end{pmatrix}, \tag{16}$$

While the implicit subsystem is given by:

$$\mathbf{f}(\mathbf{q})^{p} = \begin{pmatrix} 0 \\ \frac{p}{M^2} \mathbb{I} \\ \mathbf{u}(\rho E + p) \end{pmatrix}. \tag{17}$$

$$\mathbf{s}(\mathbf{q})^p = \begin{pmatrix} 0 \\ \frac{\rho}{\rho^{hyd}} \frac{\nabla p^{hyd}}{M^2} \\ 0 \end{pmatrix}. \tag{18}$$

Note that the gravitational source term is grouped together with the implicit subsystem to ensure the *well-balanced property* at the discrete level.

3.2   Time semi-discrete semi-implicit scheme

Based on this splitting, the semi-discrete scheme can be written as:

$$\frac{\partial \mathbf{q}}{\partial t} + \nabla \cdot \mathbf{f^u}(\mathbf{q}) + \nabla \cdot \mathbf{f}^p(\mathbf{q}) = \mathbf{s}(\mathbf{q}). \tag{19}$$

For clarity, the scheme is derived first-order in time, before extending it to second-order in Section 3.5.

The resulting first-order time semi-discrete scheme reads:

$$\rho^{n+1} - \rho^n + \Delta t \nabla \cdot (\rho \mathbf{u})^n = 0, \tag{20a}$$

$$\rho \mathbf{u}^{n+1} - \rho \mathbf{u}^n + \Delta t \nabla \cdot (\rho \mathbf{u} \otimes \mathbf{u})^n + \frac{\Delta t}{M^2} \nabla p^{n+1} = \frac{\rho^{n+1}}{\rho^{hyd}} \frac{\Delta t}{M^2} \nabla p^{hyd}, \tag{20b}$$

$$\rho E^{n+1} - \rho E^n + \Delta t \nabla \cdot \left(\rho \mathbf{u}^{n+1} \left(\frac{\rho E^n + p^n}{\rho^n} \right) \right) = 0. \tag{20c}$$

Here, the total energy flux has been time-linearized following the approach of [5], yielding a linear dependence on $\mathbf{q}^{n+1}$. This ensures that the implicit step does not involve nonlinear solves.

We define the total enthalpy as

$$H^n = \frac{\rho E^n + p^n}{\rho^n}. \tag{21}$$

The structure of the scheme is then given as follows:

We first compute the explicit stage associate to $\mathbf{f^u}$ given by:

$$\rho^{(1)} = \rho^n - \Delta t \nabla \cdot (\rho \mathbf{u})^n, \tag{22a}$$

$$\rho \mathbf{u}^{(1)} = \rho \mathbf{u}^n - \Delta t \nabla \cdot (\rho \mathbf{u} \otimes \mathbf{u})^n, \tag{22b}$$

$$\rho E^{(1)} = \rho E^n. \tag{22c}$$

Next, we compute the pressure-gravity sub-system by first deriving one implicit equation for the total energy, from which then the momentum equation is updated.

Note that the density is entirely determined by the explicit step, thus we have $\rho^{n+1} = \rho^{(1)}$. Thus, the only unknowns in the pressure sub-system are $\rho \mathbf{u}^{n+1}$ and ρE^{n+1} which reads

$$\rho \mathbf{u}^{n+1} = \rho \mathbf{u}^{(1)} - \frac{\Delta t}{M^2} \nabla p^{n+1} + \frac{\rho^{n+1}}{\rho^{hyd}} \frac{\Delta t}{M^2} \nabla p^{hyd}, \tag{23a}$$

$$\rho E^{n+1} = \rho E^{(1)} - \Delta t \nabla \cdot \left((\rho \mathbf{u})^{n+1} H^n \right). \tag{23b}$$

Inserting (23a) into (23b), we obtain the following linear implicit equation for the total energy:

$$\rho E^{n+1} = \rho E^{(1)} - \Delta t \nabla \cdot \left(H^n \rho \mathbf{u}^{(1)} \right) + \frac{\Delta t^2}{M^2} \nabla \cdot \left(H^n \nabla p^{n+1} \right) - \frac{\Delta t^2}{M^2} \nabla \cdot \left(H^n \frac{\rho^{n+1}}{\rho^{\text{hyd}}} \nabla p^{\text{hyd}} \right). \quad (24)$$

From this part the semi-implicit scheme can be formulated in two equivalent but structurally different ways:

- In the **energy-based approach**, the total energy is updated implicitly in a closed form (24), and the pressure is then obtained from the (**EOS**).

- In the **pressure-based approach**, (24) is rewritten in terms of the pressure by using the EOS which results again in an elliptic problem similar to (24) for the pressure, and the total energy is subsequently updated using the known pressure.

3.2.1 Energy-based approach

Using this time-linearization of EOS:

$$p^{n+1} = (\gamma - 1)(\rho E^{n+1} - M^2(\rho E_{\text{kin}}^n) - \frac{M^2}{Fr^2}(\rho E_{\text{pot}}^{n+1})). \quad (25)$$

where:

$$\rho E_{\text{kin}}^n = \frac{1}{2}\rho \| (\mathbf{u}^n) \|^2, \qquad \rho E_{\text{pot}}^{n+1} = \rho^{n+1}\phi. \quad (26)$$

In this approach, the pressure is eliminated from (24) by substituting its time-linear definition (25) into equation (24). After rearranging the terms, we obtain the following linear implicit problem for the total energy:

$$\rho E^{n+1} - (\gamma - 1)\frac{\Delta t^2}{M^2} \nabla \cdot \left(H^n \nabla \rho E^{n+1} \right) = \rho E^{(1,\star)}, \quad (27)$$

Where the right-hand side is given by

$$\begin{aligned}
\rho E^{(1,\star)} = \rho E^{(1)} &- \Delta t \, \nabla \cdot \left((\rho \mathbf{u})^{(1)} H^n \right) \\
&- \frac{\Delta t^2}{M^2} \nabla \cdot \left(\frac{\rho^{n+1}}{\rho^{\text{hyd}}} \nabla p^{\text{hyd}} \, H^n \right) \\
&- (\gamma - 1)\frac{\Delta t^2}{M^2} \nabla \cdot \left(H^n \, \nabla \left(M^2(\rho E_{\text{kin}})^n + \tfrac{M^2}{Fr^2}(\rho E_{\text{pot}})^{n+1} \right) \right).
\end{aligned} \quad (28)$$

Once the update of the total energy is available, the momentum equation (23a) can be advanced in time using the definition of the pressure at t^{n+1}, see (25). At this stage, the new momentum $\rho \mathbf{u}^{n+1}$ is known, and it can be re-inserted into the fully implicit flux formulation (23b) in order to recompute the total energy consistently with the new velocity field. This ensures conservation and compatibility of the fluxes with the updated solution.

Although the elliptic step already provides an approximation of ρE, but this value is only a predictor obtained through a linearization of the energy flux. While sufficient

to advance the momentum equation, it does not fully capture the coupling of pressure, velocity, and gravity at the new time level. Recomputing the energy with the updated momentum enforces consistency between mechanical variables and the thermodynamic state, preserving conservation and hydrostatic balance. Without this correction, small mismatches between energy and momentum could accumulate, degrading the well-balanced property and reducing accuracy, especially in stiff pressure–gravity regimes.

This energy-based approach thus provides a self-consistent update of both the total energy and the momentum. It concludes the derivation of the well-balanced semi-implicit time semi-discrete scheme.

3.2.2   Pressure-based approach

Using this time-linearization of EOS:

$$p^{n+1} = (\gamma - 1)(\rho E^{n+1} - M^2(\rho E_{\text{kin}}^n) - \frac{M^2}{Fr^2}(\rho E_{\text{pot}}^n)). \tag{29}$$

Where:

$$\rho E_{\text{kin}}^n = \frac{1}{2}\rho\|(\mathbf{u}^n)\|^2, \qquad \rho E_{\text{pot}}^n = \rho^n \phi. \tag{30}$$

This approach is obtained by keeping the pressure as the primary unknown. From the relation (29), the total energy at the new time step can be expressed in terms of the pressure as:

$$\rho E^{n+1} = \frac{p^{n+1}}{\gamma - 1} + M^2(\rho E_{\text{kin}})^n + \frac{M^2}{Fr^2}(\rho E_{\text{pot}})^n. \tag{31}$$

Inserting this relation into (24) leads to the following elliptic equation for the pressure:

$$p^{n+1} - (\gamma - 1)\frac{\Delta t^2}{M^2}\nabla \cdot \left(H^n \nabla p^{n+1}\right) = p^{(1,\star)}, \tag{32}$$

With the right-hand side given by

$$p^{(1,\star)} = p^{(1)} - (\gamma - 1)\Delta t\, \nabla \cdot \left(H^n \rho \mathbf{u}^{(1)}\right) - (\gamma - 1)\frac{\Delta t^2}{M^2}\nabla \cdot \left(H^n \frac{\rho^{n+1}}{\rho^{\text{hyd}}}\nabla p^{\text{hyd}}\right). \tag{33}$$

Once the pressure field is determined, the momentum equation (23a) is updated accordingly.

At this stage, we can compute a predicted value of enthalpy by first calculating the total energy as:

$$\rho \tilde{E}^{n+1} = \frac{p^{n+1}}{\gamma - 1} + M^2 \frac{1}{2}\frac{(\rho\mathbf{u})^{n+1} \cdot (\rho\mathbf{u})^{n+1}}{\rho^{n+1}} + \frac{M^2}{Fr^2}(\rho E_{\text{pot}})^{n+1}, \tag{34}$$

Which naturally defines the predicted enthalpy:

$$\tilde{H}^{n+1} = \frac{\rho \tilde{E}^{n+1} + p^{n+1}}{\rho^{n+1}}. \tag{35}$$

Finally, the total energy is updated consistently using the fully implicit flux formulation (23b):

$$\rho E^{n+1} = \rho E^n - \Delta t \, \nabla \cdot \left((\rho \mathbf{u})^{n+1} \tilde{H}^{n+1} \right). \tag{36}$$

This pressure-based closure thus provides an alternative formulation of the semi-implicit scheme, where the elliptic problem is solved directly for the pressure instead of the total energy, while still guaranteeing a well-balanced and asymptotic-preserving discretization.

3.2.3   Comparison between formulations

Both formulations evolve the conserved state vector $\mathbf{q} = (\rho, \, \rho \mathbf{u}, \, E)^\top$. The distinction lies in how the EOS is linearised and which variable is chosen as the *primary unknown* in the implicit correction.

- **Energy-based scheme.** The elliptic problem (24) is solved directly for the total energy E^{n+1}, using the linearised EOS (25). Pressure is then recovered from the updated conservative variables. This yields a consistent implicit update of both energy and momentum, at the price of an additional correction step to ensure compatibility of fluxes and conservation. also this scheme couples energy and gravity at the new time level (through $\rho E_{\text{pot}}^{n+1}$), which enhances robustness in low-Mach,

- **Pressure-based scheme.** Equation (24) is first rewritten in terms of pressure via the EOS (29), leading to the elliptic problem (32) for p^{n+1}. Once pressure is known, the momentum is updated and the total energy is reconstructed. Pressure is the *primary implicit variable* in this formulation. but this scheme freezes potential energy at the old time level (through ρE_{pot}^n). This leads to a simpler elliptic problem for pressure, closer in spirit to incompressible solvers. However, in practice this scheme has shown higher sensitivity to non-positivity and stability issues, particularly at low Mach number and fine resolutions.

3.3   Verification of the well-balanced property

An essential requirement of the proposed scheme is that it preserves hydrostatic equilibria exactly at the discrete level. We now verify this property for both approachs.

Energy-based approach

Assume that at time t^n the solution corresponds to a hydrostatic state:

$$\mathbf{u}^n = 0, \qquad \rho^n = \rho^{\text{hyd}}, \qquad p^n = p^{\text{hyd}}.$$

From the explicit stage, it follows directly that $\rho^{n+1} = \rho^{\text{hyd}}$. and with replacing ρE^n and ρE^{n+1} with its following definitions in (24):

$$\rho E^n = \frac{p^n}{\gamma - 1} + \frac{M^2}{Fr^2}(\rho E_{\text{pot}})^n, \tag{37a}$$

$$\rho E^{n+1} = \frac{p^{n+1}}{\gamma - 1} + \frac{M^2}{Fr^2}(\rho E_{\text{pot}})^{n+1}, \tag{37b}$$

$$\tag{37c}$$

So The implicit subsystem then reduces to:

$$\rho \mathbf{u}^{n+1} = -\frac{\Delta t}{M^2}\nabla\left(p^{n+1} - p^{\text{hyd}}\right), \tag{38a}$$

$$\frac{p^{n+1}}{\gamma - 1} + \frac{M^2}{Fr^2}\rho^{\text{hyd}}\phi = \frac{p^{\text{hyd}}}{\gamma - 1} + \frac{M^2}{Fr^2}\rho^{\text{hyd}}\phi - \Delta t\,\nabla\cdot\left((\rho\mathbf{u})^{n+1}H^n\right), \tag{38b}$$

We have $H^n = H^{\text{hyd}} = \frac{\gamma p^{\text{hyd}}}{\gamma-1} + \frac{M^2}{Fr^2}\rho^{\text{hyd}}\phi > 0$.
Equation (38b) is equivalent to:

$$p^{n+1} = p^{\text{hyd}} - (\gamma - 1)\Delta t\,\nabla\cdot\left((\rho\mathbf{u})^{n+1}H^n\right).$$

Inserting the momentum relation (38a), we obtain:

$$(p^{n+1} - p^{\text{hyd}}) - (\gamma - 1)\frac{\Delta t^2}{M^2}\nabla\cdot\left(H^n\nabla(p^{n+1} - p^{\text{hyd}})\right) = 0.$$

With appropriate boundary conditions, e.g. $p = p^{\text{hyd}}$ on $\partial\Omega$, the solution is $p^{n+1} = p^{\text{hyd}}$. It follows immediately that $\rho\mathbf{u}^{n+1} = 0$, hence $\mathbf{u}^{n+1} = 0$, and that $\rho E^{n+1} = \rho E^n$. Therefore, the hydrostatic equilibrium is preserved exactly at the discrete level, which completes the proof of well-balancing for the energy-based scheme.

Pressure-based approach

The argument is similar. Starting from the hydrostatic state $\mathbf{u}^n = 0$, $\rho^n = \rho^{\text{hyd}}$, and $p^n = p^{\text{hyd}}$, we again obtain $\rho^{n+1} = \rho^{\text{hyd}}$ because the explicit parts of both schemes coincide.
    The implicit subsystem then reduces to:

$$\rho \mathbf{u}^{n+1} = -\frac{\Delta t}{M^2}\nabla\left(p^{n+1} - p^{\text{hyd}}\right), \tag{39a}$$

$$\frac{p^{n+1}}{\gamma - 1} + \frac{M^2}{Fr^2}\rho^{\text{hyd}}\phi = \frac{p^{\text{hyd}}}{\gamma - 1} + \frac{M^2}{Fr^2}\rho^{\text{hyd}}\phi - \Delta t\,\nabla\cdot\left((\rho\mathbf{u})^{n+1}H^n\right), \tag{39b}$$

The pressure update then reduces to:

$$(p^{n+1} - p^{\text{hyd}}) - (\gamma - 1)\frac{\Delta t^2}{M^2}\nabla\cdot\left(H^n\nabla(p^{n+1} - p^{\text{hyd}})\right) = 0.$$

As before, with boundary conditions $p = p^{\text{hyd}}$ on $\partial\Omega$, the unique solution is $p^{n+1} = p^{\text{hyd}}$.

Substituting back into the momentum equation (39a) immediately yields $\rho\mathbf{u}^{n+1} = 0$. Hence the scheme exactly preserves the hydrostatic equilibrium also in the pressure-based formulation.

This analysis confirms that both approachs are well-balanced, thereby ensuring that hydrostatic equilibria are preserved exactly by the semi-implicit discretization.

3.4   Fully discrete scheme

For the space discretization we use a finite volume framework, where the computational domain $\Omega \subset \mathbb{R}^2$ is partitioned into non-overlapping rectangular cells Ω_K where the edge between two cells Ω_L and Ω_R is denoted by $\partial\Omega_{LR}$ and its length by $|\partial\Omega_{LR}|$.

The set of neighbours of Ω_L is denoted by $\mathcal{N}_L$ and the associated unit normal vector pointing from cell Ω_L to Ω_R is denoted by $\mathbf{n}_{LR}$. Consequently $\mathbf{n}_{LR} = -\mathbf{n}_{RL}$.

The cell-average values are defined as:

$$\mathbf{q}_L(t) = \frac{1}{|\Omega_L|} \int_{\Omega_L} \mathbf{q}(\mathbf{x}, t)d\mathbf{x}, \quad \mathbf{x} = (\mathbf{x}_1, \mathbf{x}_2). \tag{40}$$

The explicitly treated sub-system (22) is discretized using Rusanov numerical fluxes $\mathbf{F^u}$ based on the flux $\mathbf{f^u}$ as follows:

$$\mathbf{q}_L^{(1)} = \mathbf{q}_L^n - \Delta t \sum_{R \in \mathcal{N}_L} \frac{|\partial\Omega_{LR}|}{|\Omega_L|} \left(\mathbf{F^u}(\mathbf{q}_{LR}^-, \mathbf{q}_{LR}^+) \cdot \mathbf{n}_{LR} \right). \tag{41}$$

To get the characteristic speeds we construct the jacobien of the explicit subsystem in 1D wihch can easily extend it to 2D.

The Jacobian in 1D is given by:

$$A(\mathbf{q}) = \frac{\partial\mathbf{F}_n^\mathbf{u}}{\partial\mathbf{q}} = \begin{pmatrix} 0 & 1 & 0 \\ -\dfrac{\rho\mathbf{u}^2}{\rho^2} & 2\dfrac{\rho\mathbf{u}}{\rho} & 0 \\ 0 & 0 & 0 \end{pmatrix} = \begin{pmatrix} 0 & 1 & 0 \\ -\mathbf{u}^2 & 2\mathbf{u} & 0 \\ 0 & 0 & 0 \end{pmatrix}.$$

The Eigenvalues are:

$$\lambda_0 = 0, \qquad \lambda_1 = \lambda_2 = u \quad \text{(with algebraic multiplicity 2).}$$

The corresponding eigenvectors are:

$$r^{(0)} = \begin{pmatrix} 0 \\ 0 \\ 1 \end{pmatrix}, \qquad r^{(1)} = \begin{pmatrix} 1 \\ u \\ 0 \end{pmatrix}.$$

Since the eigenvalue $\lambda = u$ has algebraic multiplicity two but only one linearly independent eigenvector, the system is *defective* and therefore only *weakly hyperbolic*.

So using $\lambda_k(\mathbf{q}) = \mathbf{u} \cdot \mathbf{n}_{LR}$ the characteristic speeds of the explicit sub-system (22) and $\lambda_{LR} = \max_k(|\lambda_k(\mathbf{q}_L)|, |\lambda_k(\mathbf{q}_R)|)$. Then the numerical fluxes are defined :

$$\mathbf{F}^{\mathbf{u}}(\mathbf{q}_{LR}^-, \mathbf{q}_{LR}^+) = \frac{1}{2}\left(\mathbf{f}^{\mathbf{u}}(\mathbf{q}_{LR}^-) + \mathbf{f}^{\mathbf{u}}(\mathbf{q}_{LR}^+)\right) - \frac{1}{2}\alpha_{LR}(\mathbf{q}_{LR}^+ - \mathbf{q}_{LR}^-). \tag{42}$$

Where:

- $\mathbf{q}_{LR}^-$ and $\mathbf{q}_{LR}^+$ are the states on the left and right sides of the interface

- $\mathbf{f}^{\mathbf{u}}(\mathbf{q}_{LR}^-)$ and $\mathbf{f}^{\mathbf{u}}(\mathbf{q}_{LR}^+)$ are the corresponding physical fluxes

In the implicit pressure-gravity sub-system, standard centred differences are applied to discretize the gradient operators. This is motivated by the fact that the artificial viscosity of the numerical scheme has to be scale independent.

Divergence operators are discretized with a central flux operator which coincides with $\mathbf{F}(\mathbf{q}_L, \mathbf{q}_R)$ but zero artificial viscosity, i.e. $\alpha_{LR} = 0$.

The nested derivatives in the energy update (24) and associated right-hand sides are discretized by the differential operator $\mathbf{H}_K(h, q)$ which takes two quantities $h(\mathbf{x})$ and $q(\mathbf{x})$ and computes a second order approximation to $\nabla \cdot (h\nabla q)$.

For a given spatial direction $\mathbf{x}_j$ on cell K it corresponds to discretizing $\partial_{\mathbf{x}_j}\left(h\,\partial_{\mathbf{x}_j}q\right)$ and it writes

$$\mathbf{H}_{j,K}(h, q) = \frac{1}{\Delta\mathbf{x}_{j,K}}\left(h_{RK}\frac{\mathbf{q}_R - \mathbf{q}_K}{|\partial\Omega_{RK}|} - h_{KL}\frac{\mathbf{q}_K - \mathbf{q}_L}{|\partial\Omega_{KL}|}\right), \tag{43}$$

Where $\Delta\mathbf{x}_{j,K}$ denotes the length of cell K in $\mathbf{x}_1$ direction and the cells L, R are the direct adjacent left and right cells in $\mathbf{x}_j$ direction.

Then the multidimensional differential operator $\mathbf{H}$ is given by $\mathbf{H} = \sum_{n=1}^d \mathbf{H}_n(h, q)$.

To ensure the well-balancing of the fully-discrete scheme, the spatial discretization of the source term has to match the discretization of the centred pressure gradient. In other words, we have to integrate

$$s_K = \frac{1}{|\Omega_K|}\int_{C_K}\frac{1}{M^2}\frac{\rho}{\rho^{\text{hyd}}}\nabla p^{\text{hyd}}d\mathbf{x} \tag{44}$$

Up to second order using centred differences for the pressure because:

- the discrete source term must exactly balance the discrete pressure gradient in hydrostatic equilibrium (*well-balancing*);

- the flux discretization in the implicit subsystem is second-order accurate, hence the source term needs the same order of accuracy for consistency;

- a first-order scheme would introduce excessive numerical diffusion and destroy hydrostatic balance in smooth regions;

- second-order accuracy is sufficient to achieve a robust and scale-independent discretization without adding unnecessary complexity.

We propose the following discretization in $\mathbf{x}_1-$direction:

$$\bar{s}_{j,K} = \frac{1}{2}\left(\left(\frac{\rho}{\rho^{\mathrm{hyd}}}\right)_{KR} + \left(\frac{\rho}{\rho^{\mathrm{hyd}}}\right)_{KL}\right)\frac{p_{RK}^{\mathrm{hyd}} - p_{KL}^{\mathrm{hyd}}}{\Delta\mathbf{x}_1}. \tag{45}$$

Where:

$$\left(\frac{\rho}{\rho^{\mathrm{hyd}}}\right)_{RK} = \frac{1}{2}\left(\left(\frac{\rho}{\rho^{\mathrm{hyd}}}\right)_{R} + \left(\frac{\rho}{\rho^{\mathrm{hyd}}}\right)_{K}\right), \quad p_{RK}^{\mathrm{hyd}} = \frac{1}{2}(p_{R}^{\mathrm{hyd}} + p_{K}^{\mathrm{hyd}}). \tag{46}$$

Thus the multi-dimensional source term is then computed as $\bar{s}_K = \sum_{n=1}^{d}\bar{s}_{n,K}$.

Due to the implicit treatment of the pressure-gravity sub-system, the CFL condition of the semi-implicit scheme is only dictated by the transport sub-system.

Therefore we have the following time step restriction

$$\Delta t \leq \nu\frac{\min_{L,K}|\partial\Omega_{LK}|}{\max_{k,K}|\lambda_k^{\mathbf{u}}(\mathbf{q}_K)|}, \tag{47}$$

where $0 < \nu < 1$ denotes the CFL number and $\lambda_k^{\mathbf{u}}$ denote the eigenvalues of the explicit transport-subsystem.

3.5   Second Order IMEX-RK scheme

To achieve Second-order accuracy extension in time we adopt implicit–explicit Runge–Kutta (IMEX-RK) methods. In particular, we follow the class of schemes introduced by Ascher, Ruuth, and Spiteri [6]. A general p-th order IMEX-RK method with s stages can be written in Butcher notation as:

$$\text{explicit part:} \quad \begin{array}{c|cccc} 0 & 0 & 0 & \cdots & 0 \\ \tilde{c}_2 & \tilde{a}_{21} & 0 & \cdots & 0 \\ \vdots & \vdots & \ddots & \ddots & \vdots \\ \tilde{c}_s & \tilde{a}_{s1} & \cdots & \tilde{a}_{s,s-1} & 0 \\ \hline & \tilde{b}_1 & \cdots & \tilde{b}_{s-1} & \tilde{b}_s \end{array} \quad \text{implicit part:} \quad \begin{array}{c|cccc} 0 & 0 & 0 & \cdots & 0 \\ c_2 & 0 & a_{22} & \cdots & 0 \\ \vdots & \vdots & \vdots & \ddots & \vdots \\ c_s & 0 & a_{s2} & \cdots & a_{ss} \\ \hline & 0 & b_2 & \cdots & b_s \end{array} \ . \tag{48}$$

The IMEX-RK scheme advances the solution by computing intermediate stage values: $\mathbf{q}^{(k)}$ according to

$$\mathbf{q}^{(k)} = \mathbf{q}^n - \Delta t\sum_{l=1}^{k-1}\tilde{a}_{kl}\,\nabla\cdot f^e(\mathbf{q}^{(l)}) - \Delta t\sum_{l=1}^{k}a_{kl}\left(\nabla\cdot f^i(\mathbf{q}^{(l)}) + s(\mathbf{q}^{(l)})\right), \tag{49a}$$

$$\mathbf{q}^{n+1} = \mathbf{q}^n - \Delta t\sum_{k=1}^{s}\tilde{b}_k\,\nabla\cdot f^e(\mathbf{q}^{(k)}) - \Delta t\sum_{k=1}^{s}b_k\left(\nabla\cdot f^i(\mathbf{q}^{(k)}) + s(\mathbf{q}^{(k)})\right). \tag{49b}$$

We define auxiliary intermediate states:

$$\mathbf{q}^{(k,\star)} = \mathbf{q}^n - \Delta t\sum_{l=1}^{k-1}\left(\tilde{a}_{kl}\,\nabla\cdot f^e(\mathbf{q}^{(l)}) + a_{kl}\left(\nabla\cdot f^i(\mathbf{q}^{(l)}) + s(\mathbf{q}^{(l)})\right)\right), \tag{50}$$

In the present work we follow the ARS(3,3,2) formulation, whose Butcher tables are given by:

$$
\text{explicit:}\quad
\begin{array}{c|cccc}
0 & 0 & 0 & 0 \\
\beta & \beta & 0 & 0 \\
1 & \beta-1 & 2-\beta & 0 \\
\hline
 & \beta-1 & 2-\beta & 0
\end{array}
\qquad
\text{implicit:}\quad
\begin{array}{c|cccc}
0 & 0 & 0 & 0 \\
\beta & 0 & \beta & 0 \\
1 & 0 & 1-\beta & \beta \\
\hline
 & 0 & 1-\beta & \beta
\end{array}, \tag{51}
$$

With the coefficient:

$$
\beta = 1 - \frac{\sqrt{2}}{2}.
$$

To obtain second-order accuracy in space, we employ a MUSCL-type linear reconstruction. For a given spatial direction $\mathbf{x}_j$ on cell k, the cell average $\mathbf{q}_{j,k}$ is reconstructed at the interface midpoints by

$$
\mathbf{q}_{j,K}^{\pm} = \mathbf{q}_{j,k} \pm \tfrac{1}{2}\,\psi(\mathbf{q}_{j+1,K} - \mathbf{q}_{j,k}, \mathbf{q}_{j,K} - \mathbf{q}_{j-1,k}),
$$

Where ψ is a slope limiter (e.g. minmod). This procedure yields second-order accuracy in smooth regions while preserving stability and monotonicity near discontinuities. The resulting interface states are then passed to the numerical flux $\mathbf{F}(\mathbf{q}_L, \mathbf{q}_R)$.

CFL condition. The timestep restriction of the IMEX-RK scheme is determined solely by the explicit transport sub-system. The stiff implicit part does not impose additional constraints. The CFL condition reads:

$$
\Delta t \le \nu\, \frac{\min_{L,K}|\partial\Omega_{LK}|}{\max_{k,K}|\lambda_k^{\mathbf{u}}(\mathbf{q}_K)|}, \qquad \nu = \frac{1}{3}\frac{1}{2d}, \tag{52}
$$

Where $\lambda_k^{\mathbf{u}}(\mathbf{q}_K)$ denote the characteristic speeds of the explicit transport system and d the spatial dimension.

4 Implementation

The numerical scheme described above has been implemented in a modular and reproducible way. The development is managed through a private `GitLab` repository.

The solver is structured as a `Python` package. The code is organized into dedicated modules for mesh handling, discretization, numerical fluxes, time integration, and post-processing. This modular design ensures flexibility, reusability, and readability of the implementation.

A set of benchmark test cases has already been implemented within the package. These test cases are fully parameterizable, allowing the user to configure the domain, boundary conditions, and numerical parameters without modifying the core code. This feature provides a convenient way to validate the scheme and benchmark different physical scenarios.

Particular attention has been paid to the implicit step required for solving the elliptic pressure equation. For this purpose, the matrix corresponding to the discretized operator

is built explicitly, enabling the use of robust preconditioners in conjunction with Krylov iterative solvers.In particular, we employed the BiCGStab solver combined with an ILU preconditioner, which significantly enhances stability and accelerates convergence in the low-Mach regime, where the elliptic system is especially stiff.

For the execution of simulations, we rely on the `Gaya` high-performance computing (HPC) cluster. The use of Gaya ensures sufficient computational resources to carry out the test cases efficiently and to test the scalability of the solver in more demanding configurations.

5   Numerical results

To validate the **well-balanced** property, **asymptotic-preserving (AP)** character, and overall **robustness** under varied flow conditions, we present a comprehensive set of numerical tests.

5.1   Well-balanced tests

For the well-balanced tests, we consider stationary atmospheric solutions in the isothermal and polytropic regimes in two dimensions, computed with the second-order scheme. Simulations are carried out on a uniform grid of 100×100 cells over the domain $[0,1] \times [0,1]$ up to a final time $T_f = 1.0$ with exact boundary.

Using **quadratic potential** functions $\phi(x,y) = \frac{1}{2}(x+y)$, $\gamma = 1.4$ for both polytropic and isothermal atmosphere.

The errors are computed as the L^1 norm of the difference between the numerical solution and the hydrostatic state:

$$\|q^h - q^{hyd}\|_{L^1} = \frac{1}{|\Omega|} \sum_{i,j} |q^h_{i,j} - q^{hyd}_{i,j}| \, \Delta x \, \Delta y.$$

5.1.1   Isothermal atmosphere

We consider the initial conditions given in (10). In the isothermal atmosphere, the hydrostatic density profile contains the exponential factor $\exp(-\frac{M^2}{Fr^2})$. If the ratio $\frac{M}{Fr}$ is too large, this exponential decays too rapidly and the density vanishes numerically. To prevent such degeneracy, one must choose values of $\frac{Fr}{M}$ tthat ensure the density remains well resolved. In our study, we investigate this criterion through different test cases with $M = Fr$, $M = 0.75\,Fr$, and $M = 10\,Fr$, which allows us to assess the robustness of the scheme under different scalings of M and Fr.

For the isothermal atmosphere, the results in Tables 1–2 confirm that both the Energy-based and Pressure-based schemes also preserve the hydrostatic state up to machine precision for all considered Mach numbers, including the sensitive cases $M = Fr$, $M = 0.75\,Fr$, and $M = 10\,Fr$. Notably, even in the challenging scenario $\frac{Fr}{M} = 0.75$, where the exponential density profile could degenerate, the errors remain at round-off level. This demonstrates the robustness of the method and its ability to handle stiff configurations induced by exponential hydrostatic profiles.

	$Fr = 0.75M$			$Fr = M$			$Fr = 10M$		
	ρ	$\|u\|$	E	ρ	$\|u\|$	E	ρ	$\|u\|$	E
$M = 1$	5.98e-13	2.26e-13	2.20e-11	4.71e-13	7.83e-14	7.25e-12	1.06e-12	2.51e-14	9.51e-13
$M = 10^{-1}$	8.67e-13	2.99e-13	2.38e-11	8.55e-13	1.58e-13	1.51e-11	9.18e-13	7.78e-15	1.85e-12
$M = 10^{-2}$	7.56e-13	1.96e-13	2.03e-11	9.63e-13	1.51e-13	1.59e-11	1.07e-12	6.94e-15	1.99e-12
$M = 10^{-3}$	6.88e-13	2.07e-13	2.02e-11	9.24e-13	1.25e-13	1.13e-11	1.36e-12	9.88e-15	2.64e-12
$M = 10^{-4}$	6.98e-13	2.67e-13	2.03e-11	9.15e-13	1.68e-13	1.60e-11	1.02e-12	7.87e-15	1.95e-12
$M = 10^{-5}$	5.34e-13	1.81e-13	1.51e-11	5.99e-13	1.01e-13	9.70e-12	1.01e-12	6.97e-15	1.95e-12
$M = 10^{-6}$	5.82e-13	2.31e-13	1.61e-11	6.35e-13	9.84e-14	1.04e-11	1.17e-12	7.31e-15	2.27e-12
$M = 10^{-7}$	8.00e-13	1.69e-13	1.21e-11	9.22e-13	1.47e-13	1.41e-11	9.99e-13	8.41e-15	2.00e-12
$M = 10^{-8}$	7.07e-13	1.89e-13	1.38e-11	9.95e-13	1.96e-13	1.87e-11	8.40e-13	6.14e-15	1.68e-12
$M = 10^{-9}$	6.41e-13	2.94e-13	2.06e-11	1.09e-12	1.81e-13	1.83e-11	1.18e-12	8.37e-15	2.27e-12
$M = 10^{-10}$	6.86e-13	2.39e-13	1.92e-11	6.84e-13	9.99e-14	9.92e-12	1.06e-12	5.17e-15	1.86e-12

Table 1: L^1 errors for isothermal atmosphere using the Energy-based approach.

	$Fr = 0.75M$			$Fr = M$			$Fr = 10M$		
	ρ	$\|u\|$	E	ρ	$\|u\|$	E	ρ	$\|u\|$	E
$M = 1$	6.36e-13	1.57e-13	1.55e-11	4.71e-13	9.36e-14	8.09e-12	1.26e-12	3.21e-14	7.70e-13
$M = 10^{-1}$	6.14e-13	2.32e-13	2.07e-11	6.03e-13	1.32e-13	1.21e-11	1.06e-12	8.01e-15	1.99e-12
$M = 10^{-2}$	5.56e-13	1.77e-13	1.68e-11	6.20e-13	1.14e-13	1.01e-11	6.53e-13	6.19e-15	1.44e-12
$M = 10^{-3}$	5.41e-13	1.64e-13	1.51e-11	5.31e-13	7.50e-14	7.80e-12	8.15e-13	8.63e-15	1.96e-12
$M = 10^{-4}$	6.85e-13	2.66e-13	1.90e-11	7.19e-13	1.17e-13	1.09e-11	5.76e-13	5.54e-15	1.26e-12
$M = 10^{-5}$	7.62e-13	1.87e-13	1.28e-11	6.51e-13	6.30e-14	5.66e-12	8.45e-13	8.66e-15	1.88e-12
$M = 10^{-6}$	6.75e-13	2.56e-13	1.73e-11	5.75e-13	6.77e-14	6.09e-12	1.09e-12	8.62e-15	2.31e-12
$M = 10^{-7}$	4.64e-13	1.38e-13	1.36e-11	6.39e-13	9.32e-14	8.10e-12	9.64e-13	9.09e-15	2.04e-12
$M = 10^{-8}$	4.74e-13	8.40e-14	8.70e-12	5.78e-13	9.48e-14	8.58e-12	7.15e-13	9.59e-15	1.66e-12
$M = 10^{-9}$	4.53e-13	8.48e-14	8.97e-12	9.08e-13	1.61e-13	1.44e-11	1.35e-12	4.74e-15	2.33e-12
$M = 10^{-10}$	5.66e-13	1.65e-13	1.59e-11	4.32e-13	7.00e-14	6.72e-12	9.96e-13	5.22e-15	1.83e-12

Table 2: L^1 errors for isothermal atmosphere using the Pressure-based approach.

5.1.2 Polytropic atmosphere

We consider the initial conditions given in (11). In the polytropic case, the positivity of the hydrostatic density requires

$$\frac{Fr}{M} \geq \sqrt{\tfrac{2}{5}} \simeq 0.63.$$

We test this atmosphere under delicate regimes with $M = Fr$, $M = 0.75\,Fr$, and $M = 10\,Fr$, in order to evaluate the robustness of the scheme when the hydrostatic balance approaches its critical limit.

For the polytropic atmosphere, the results in Tables 3–4 show that both the Energy-based and Pressure-based formulations successfully preserve the hydrostatic equilibrium with errors at the level of machine precision across all Mach numbers tested, including the delicate scalings.

Even in the vicinity of the theoretical positivity constraint $\frac{Fr}{M} \geq \sqrt{\tfrac{2}{5}}$, the schemes remain stable and accurate, highlighting their well-balanced nature and robustness in stiff regimes.

	$Fr = 0.75M$			$Fr = M$			$Fr = 10M$		
	ρ	$\|u\|$	E	ρ	$\|u\|$	E	ρ	$\|u\|$	E
$M = 1$	5.91e-13	2.14e-13	1.67e-11	1.17e-12	2.10e-13	1.69e-11	1.04e-12	2.66e-14	9.93e-13
$M = 10^{-1}$	8.25e-13	2.62e-13	2.02e-11	9.65e-13	1.24e-13	1.04e-11	8.56e-13	9.35e-15	1.96e-12
$M = 10^{-2}$	8.76e-13	3.03e-13	2.28e-11	7.21e-13	8.42e-14	6.92e-12	1.04e-12	4.46e-15	1.81e-12
$M = 10^{-3}$	1.04e-12	2.99e-13	1.66e-11	7.21e-13	8.42e-14	6.92e-12	8.40e-13	7.26e-15	1.75e-12
$M = 10^{-4}$	5.59e-13	1.46e-13	8.32e-12	7.49e-13	1.52e-13	1.27e-11	8.40e-13	1.05e-14	1.74e-12
$M = 10^{-5}$	7.74e-13	3.09e-13	1.82e-11	7.48e-13	1.38e-13	1.20e-11	1.11e-12	8.49e-15	2.17e-12
$M = 10^{-6}$	7.33e-13	2.95e-13	1.70e-11	7.92e-13	1.72e-13	1.34e-11	1.09e-12	1.09e-14	2.16e-12
$M = 10^{-7}$	7.16e-13	3.00e-13	1.62e-11	7.88e-13	1.48e-13	1.22e-11	9.50e-13	9.98e-15	1.93e-12
$M = 10^{-8}$	7.78e-13	2.02e-13	1.12e-11	6.52e-13	1.36e-13	1.14e-11	8.35e-13	8.23e-15	1.76e-12
$M = 10^{-9}$	5.80e-13	2.69e-13	1.51e-11	9.21e-13	1.58e-13	1.34e-11	1.03e-12	1.07e-14	2.11e-12
$M = 10^{-10}$	6.32e-13	2.99e-13	1.67e-11	1.08e-12	1.78e-13	1.57e-11	9.44e-13	9.60e-15	1.71e-12

Table 3: L^1 errors for polytropic atmosphere using the Energy-based approach.

	$Fr = 0.75M$			$Fr = M$			$Fr = 10M$		
	ρ	$\|u\|$	E	ρ	$\|u\|$	E	ρ	$\|u\|$	E
$M = 1$	6.31e-13	1.58e-13	1.22e-11	7.17e-13	6.35e-14	4.91e-12	6.57e-13	1.37e-14	4.43e-13
$M = 10^{-1}$	4.75e-13	1.70e-13	1.28e-11	4.30e-13	7.47e-14	6.01e-12	6.35e-13	5.72e-15	1.39e-12
$M = 10^{-2}$	6.95e-13	2.06e-13	1.69e-11	4.31e-13	4.71e-14	3.78e-12	1.13e-12	6.52e-15	2.16e-12
$M = 10^{-3}$	5.22e-13	8.55e-14	1.10e-11	8.57e-13	1.44e-13	1.16e-11	1.13e-12	5.69e-15	2.29e-12
$M = 10^{-4}$	4.98e-13	1.22e-13	1.30e-11	7.72e-13	1.21e-13	9.70e-12	6.07e-13	5.01e-15	1.39e-12
$M = 10^{-5}$	5.93e-13	1.08e-13	1.19e-11	7.33e-13	1.39e-13	1.09e-11	1.19e-12	6.48e-15	2.36e-12
$M = 10^{-6}$	3.12e-13	5.31e-14	6.15e-12	9.78e-13	1.83e-13	1.42e-11	1.14e-12	7.79e-15	2.41e-12
$M = 10^{-7}$	4.70e-13	9.69e-14	1.16e-11	6.18e-13	1.04e-13	8.16e-12	7.59e-13	5.40e-15	1.60e-12
$M = 10^{-8}$	6.75e-13	1.12e-13	1.21e-11	5.99e-13	1.10e-13	8.65e-12	1.09e-12	5.10e-15	2.14e-12
$M = 10^{-9}$	5.21e-13	9.40e-14	1.09e-11	4.79e-13	8.04e-14	6.67e-12	1.41e-12	8.09e-15	2.95e-12
$M = 10^{-10}$	4.70e-13	7.05e-14	9.15e-12	7.55e-13	6.90e-14	5.46e-12	4.31e-13	5.35e-15	1.14e-12

Table 4: L^1 errors for polytropic atmosphere using the Pressure-based approach.

5.2 Accuracy

To assess the accuracy and asymptotic preserving (AP) properties of the proposed schemes, we employ the Gresho vortex in a gravitational field, taken from [4]. This benchmark combines a nontrivial hydrostatic equilibrium with a rotating incompressible flow. It is particularly suited to evaluate the scheme's well-balancedness, robustness in the low Mach regime, and experimental order of convergence (EOC).

5.2.1 Graf-Gresho vortex with gravity

Following [4] the initial condition is constructed in polar coordinates to satisfy:

$$\frac{1}{M^2}\partial_r p = \rho \frac{u_\theta^2}{r} - \frac{\rho}{Fr^2}\partial_r \phi, \tag{53}$$

where the total pressure is split into a hydrostatic component p_0 and a vortex-induced perturbation p_2:

$$p(r) = p_0(r) + M^2 p_2(r), \qquad p_0 = RT\rho, \qquad \rho = \exp\left(-\frac{M^2}{Fr^2 RT}\phi(r)\right). \tag{54}$$

The angular velocity profile is defined as:

$$u_\theta(r) = \frac{1}{u_r}\begin{cases} 5r, & r \le 0.2, \\ 2 - 5r, & 0.2 < r \le 0.4, \\ 0, & r > 0.4. \end{cases}$$

The gravitational potential $\phi(r)$ is chosen to be smooth and constant at the domain boundaries to ensure periodicity:

$$\phi(r) = \begin{cases} 12.5\, r^2, & r \le 0.2, \\ 0.5 - \ln(0.2) + \ln(r), & 0.2 < r \le 0.4, \\ \ln(2) - \dfrac{0.5\, r_c}{r_c - 0.4} + \dfrac{2.5\, r_c\, r}{r_c - 0.4} - \dfrac{1.25\, r^2}{r_c - 0.4}, & 0.4 < r \le r_c, \\ \ln(2) - \dfrac{0.5\, r_c}{r_c - 0.4} + \dfrac{1.25\, r_c^2}{r_c - 0.4}, & r > r_c. \end{cases} \tag{55}$$

The pressure perturbation $p_2(r)$ due to centrifugal forces is given by:

$$p_2(r) = \frac{Fr^2 RT}{M^2 u_r^2}\begin{cases} p_2^{(1)}(r), & r \le 0.2, \\ p_2^{(1)}(0.2) + p_2^{(2)}(r), & 0.2 < r \le 0.4, \\ p_2^{(1)}(0.2) + p_2^{(2)}(0.4), & r > 0.4, \end{cases}$$

with the auxiliary functions:

$$p_2^{(1)}(r) = 1 - \exp\left(-\frac{12.5\, r^2}{M^2/(Fr^2 RT)}\right),$$

$$p_2^{(2)}(r) = \frac{1}{(Fr^2 RT - M^2)(Fr^2 RT - 0.5M^2)} \cdot \exp\left(\frac{(-0.5 + \ln(0.2))M^2}{Fr^2 RT}\right).$$

$$\left[r^{\frac{M^2}{Fr^2 RT}}\left(M^4(r(10 - 12.5r) - 2) - 4Fr^4(RT)^2 + Fr^2 M^2 RT(r(12.5r - 20) + 6)RT\right) \right.$$

$$\left. + \exp\left(\frac{-\ln(0.2)M^2}{Fr^2 RT}\right)\left(4Fr^4 R^2 T^2 - 2.5Fr^2 M^2 RT + 0.5M^4\right) \right].$$

The velocity components are initialized using $\theta = \arctan 2(y, x)$ as:

$$\mathbf{u}(x, y) = u_\theta(r)\, \mathbf{e}_\theta = u_\theta(r)\begin{pmatrix} -\sin(\theta) \\ \cos(\theta) \end{pmatrix}. \tag{56}$$

The reference values used for non-dimensionalization are:

$$x_r = 1\,\text{m}, \quad \rho_r = 1\,\text{kg/m}^3, \quad u_r = 2 \cdot 0.2\pi\,\text{m/s}, \quad t_r = \frac{1}{u_r}, \quad RT = \frac{1}{M^2}.$$
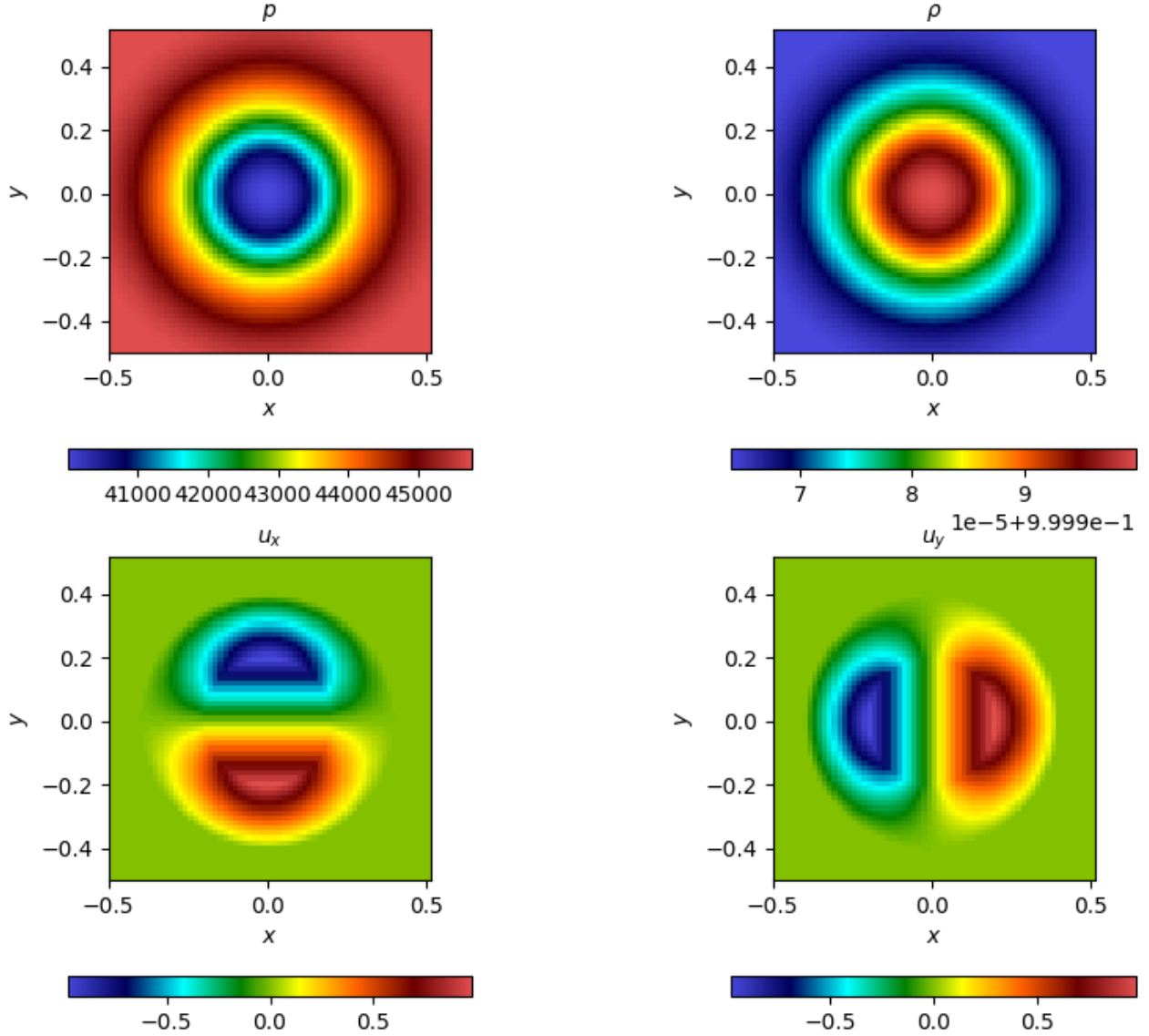
Figure 1: initial state for $M = Fr = 10^{-2}$ at $t = 0$

In Figures 2 3, we present simulations performed on the domain $[0, 1] \times [0, 1]$ with periodic boundary conditions. The computations use a final time $T_f = 1$ which corresponds to one turn of the vortex, an adiabatic index $\gamma = 1.4$, and parameters $M = Fr = 10^{-2}$ on a 128×128 uniform grid.

The results show that in the *energy-based scheme*, the vortex structure is well preserved over time, with the pressure, density, and velocity fields remaining consistent with the initial condition (Figure 1). This confirms that the method accurately captures the delicate balance between pressure gradients and centrifugal forces in this low-Mach configuration.

In contrast, the *pressure-based scheme* (Figure 3) develops visible spurious oscillations, highlighting its sensitivity to stability issues.
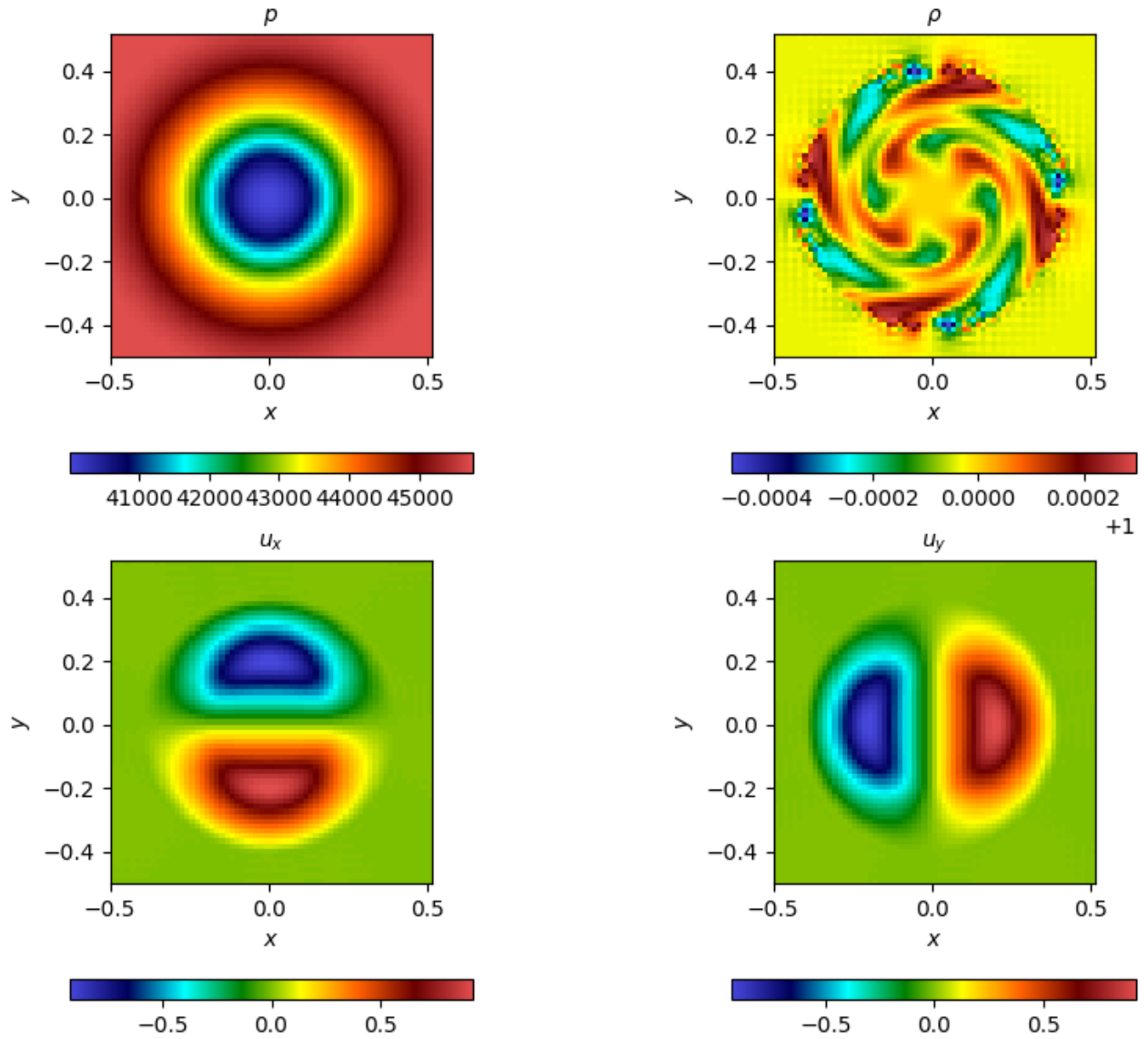
Figure 2: Graf-Gresho vortex for $M = Fr = 10^{-2}$ at $t = 1$ using Energy-based approach

Note: In our simulations, we encountered stability issues with the pressure-based formulation starting from $M = 10^{-2}$. For this reason, in the following we restrict the analysis to the energy-based formulation only.
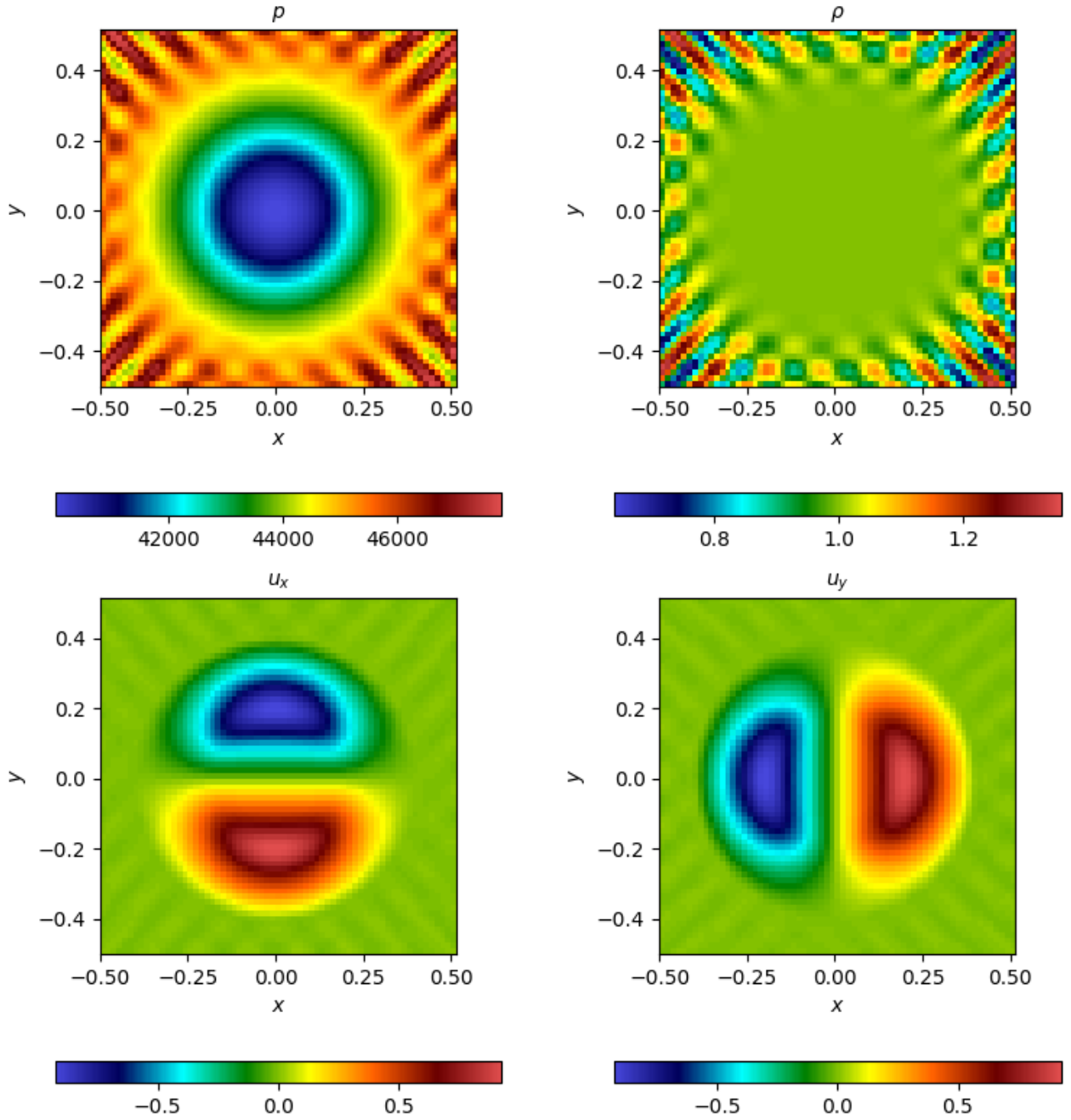
Figure 3: Graf-Gresho vortex for $M = Fr = 10^{-2}$ at $t = 1$ using Pressure-based approach

In Figure 4, we display the initial Mach number distribution for the Graf-Gresho vortex at $M = 10^{-2}$. The distribution shows that the flow is initially well structured, with the Mach number remaining small, consistent with the low-Mach regime.

Figure 5 presents the Mach number distribution at final time $t = 1$ for different maximal Mach numbers ranging from $M = 10^{-1}$ down to $M = 10^{-4}$. The results illustrate how decreasing the Mach number enhances the stiffness of the problem, while the scheme successfully maintains the vortex structure and captures the correct scaling of the Mach distribution across all tested regimes.
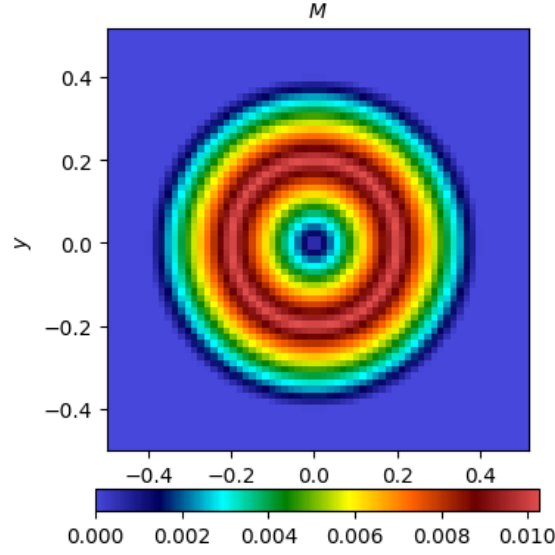
Figure 4: Initial Mach number distribution for $M = 10^{-2}$

We perform a convergence study for various Mach numbers by evaluating the L^1 errors in density, momentum, and total energy on a sequence of refined uniform grids, as shown in Table 5. The results demonstrate that the Energy-based scheme achieves close to second-order accuracy across all conserved quantities, which provides compelling evidence of the scheme's asymptotic preserving (AP) properties and numerical robustness.

Moreover, the vortex structure remains coherent during the simulation, and the kinetic energy loss is both minimal and nearly insensitive to the Mach number. These observations confirm the accuracy and stability of the proposed method in the low Mach number regime.

M	Fr	N	ρ		ρU_x		ρU_y		ρE	
10^{-1}	10^{-1}	25	8.230E-04	–	1.058E-02	–	1.058E-02	–	1.379E-03	–
		50	1.648E-04	2.32	2.681E-03	1.98	2.681E-03	1.98	2.016E-04	2.77
		100	4.111E-05	2.00	1.000E-03	1.42	1.000E-03	1.42	5.650E-05	1.83
		200	1.130E-05	1.86	3.593E-04	1.48	3.593E-04	1.48	2.240E-05	1.34
10^{-2}	10^{-2}	25	6.559E-04	–	1.025E-02	–	1.025E-02	–	1.229E-03	–
		50	1.168E-04	2.49	2.622E-03	1.97	2.622E-03	1.97	1.320E-04	3.22
		100	3.101E-05	1.91	9.884E-04	1.41	9.884E-04	1.41	2.809E-05	2.23
		200	8.746E-06	1.83	3.565E-04	1.47	3.565E-04	1.47	8.093E-06	1.80
10^{-3}	10^{-3}	25	6.424E-04	–	1.022E-02	–	1.022E-02	–	1.261E-03	–
		50	9.818E-05	2.71	2.622E-03	1.96	2.622E-03	1.96	1.188E-04	3.41
		100	2.528E-05	1.96	9.879E-04	1.41	9.879E-04	1.41	2.495E-05	2.25
		200	7.423E-06	1.77	3.565E-04	1.47	3.565E-04	1.47	7.532E-06	1.73
10^{-4}	10^{-4}	25	6.427E-04	–	1.022E-02	–	1.022E-02	–	1.262E-03	–
		50	9.876E-05	2.70	2.622E-03	1.96	2.622E-03	1.96	1.189E-04	3.41
		100	2.545E-05	1.96	9.880E-04	1.41	9.880E-04	1.41	2.497E-05	2.25
		200	7.387E-06	1.78	3.565E-04	1.47	3.565E-04	1.47	7.514E-06	1.73

Table 5: L^1 errors and convergence rates for various values of M and Fr using the Energy-based scheme.

(a) $M = 10^{-1}$

(b) $M = 10^{-2}$

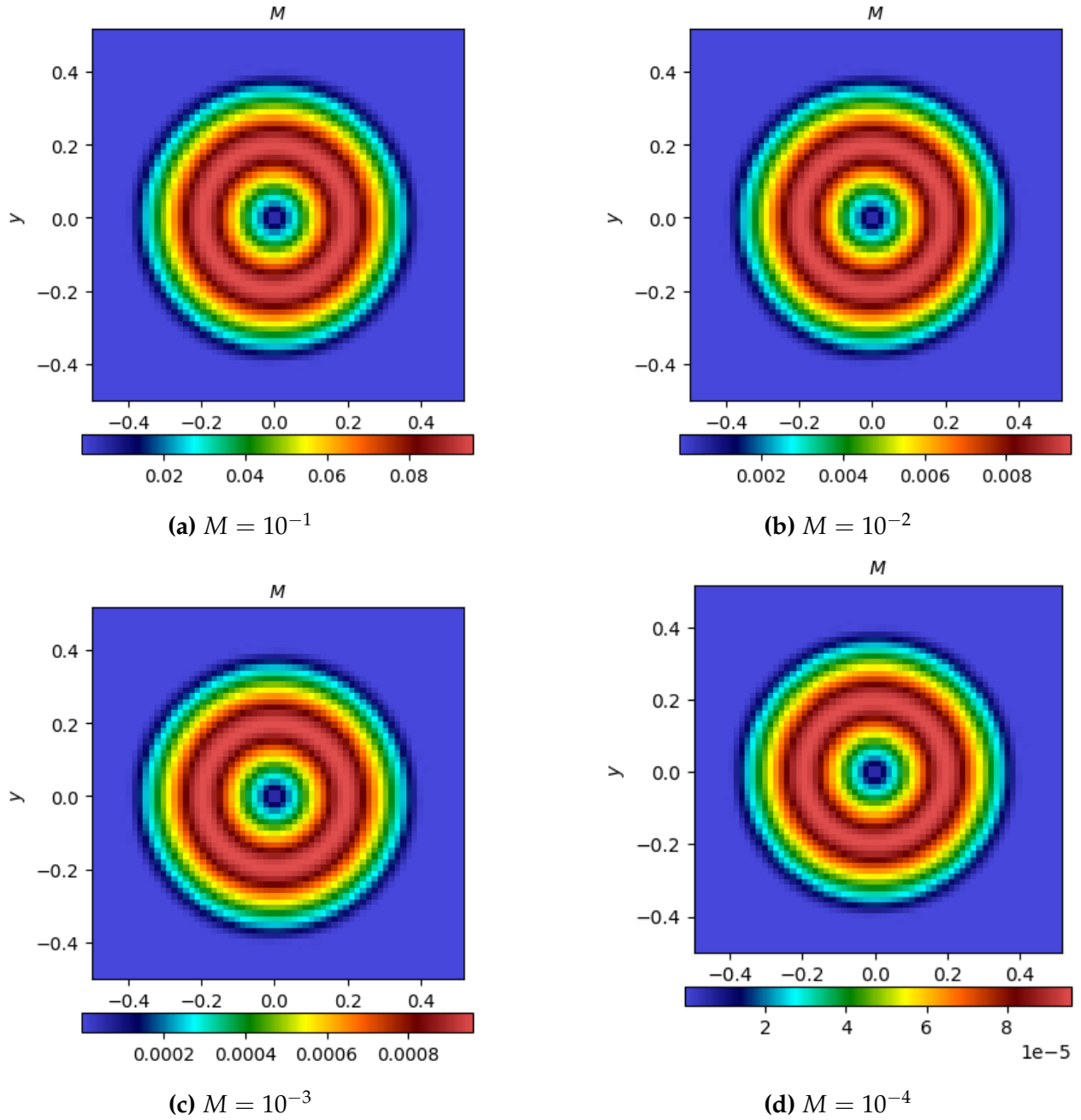**(c)** $M = 10^{-3}$

(d) $M = 10^{-4}$

Figure 5: Mach number distribution for different maximal Mach numbers at $t = 1$

Figure 6 complements these results by illustrating the loss of kinetic energy after one full vortex turn. The curves exhibit a clear trend of reduced dissipation with increasing grid resolution, while the effect of the Mach number is negligible. This indicates that the scheme maintains good accuracy and consistency for a wide range of Mach numbers, with grid refinement being the dominant factor controlling dissipation errors.
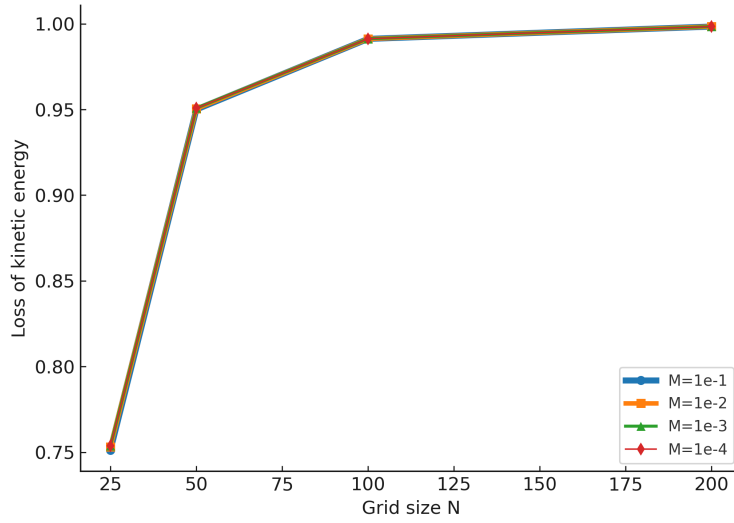
Figure 6: Loss of kinetic energy for different grids and Mach numbers after one full turn of the vortex

5.3   Limit vanishing gravitational source term (Euler equations)

5.3.1   Sod shock tube problem

The Sod shock tube test is a classical one-dimensional Riemann problem [7] and serves as a standard benchmark for hyperbolic conservation laws. It consists of two constant states separated by a discontinuity at $x = 0.5$ on the domain $[0, 1]$, with initial conditions:

$$(\rho, u, p)(x, 0) = \begin{cases} (1.0, 0.0, 1.0), & x < 0.5, \\ (0.125, 0.0, 0.1), & x > 0.5, \end{cases}$$

with adiabatic index $\gamma = 1.4$, Mach number $M = 1$ and final time $t = 0.1644$.

The domain is discretized using $N_x = 75$ cells. The reference (exact) solution is obtained from the open-source Riemann solver available at `https://github.com/pmocz/riemann-solver`.

This initial discontinuity evolves into the characteristic wave pattern of the Euler equations: a rarefaction wave propagating to the left, a contact discontinuity in the middle, and a shock wave moving to the right.

From figure 7 we can see that both the energy-based and pressure-based schemes yield results that are nearly indistinguishable from each other and from the exact solution. The shock wave, contact discontinuity, and rarefaction fan are all accurately captured. As expected, the contact discontinuity is slightly smeared due to numerical diffusion, but the shock position and amplitude remain in excellent agreement with the reference solution.
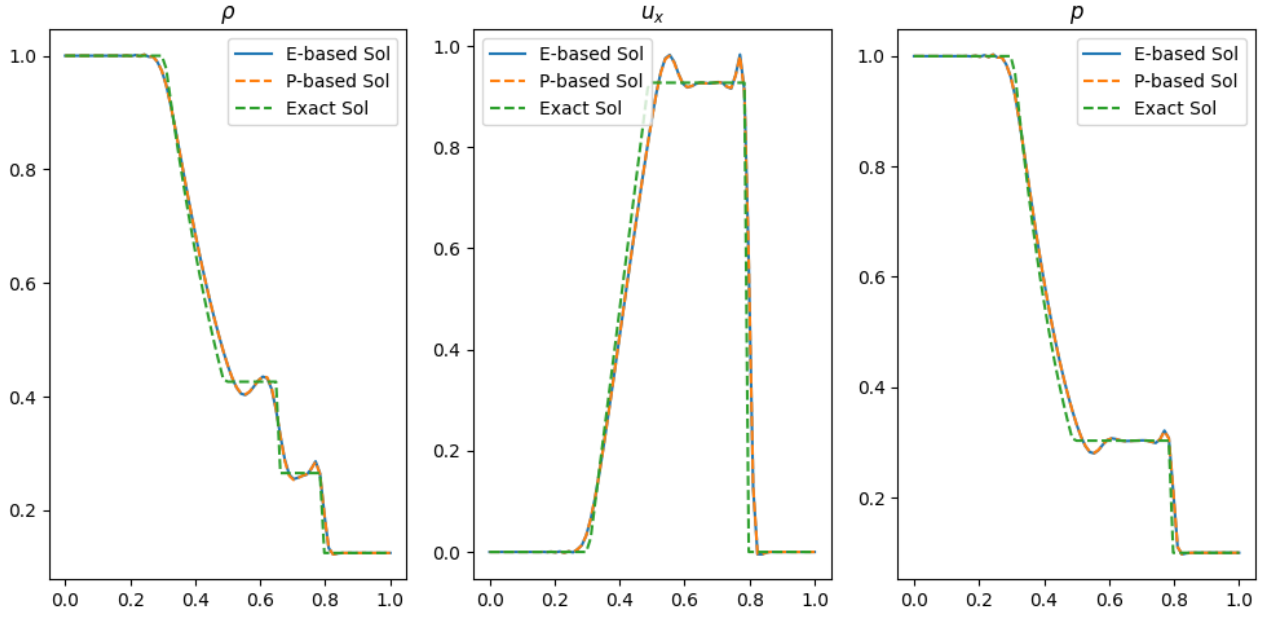
Figure 7: Numerical vs exact solution for the Sod shock tube problem at $t = 0.1644$ with $N_x = 75$ cells.

5.3.2   Kelvin-Helmholtz instability

The Kelvin–Helmholtz instability arises when there is a velocity shear across the interface between two fluids of different densities. Even if the fluids are initially in pressure equilibrium, the shear layer becomes unstable, generating vortices that roll up and evolve into turbulence.

We adopt the smooth formulation of the Kelvin–Helmholtz instability introduced in [8]. The computational domain is $\Omega = [0,1] \times [0,1]$ with periodic boundary conditions in both directions, and constant initial pressure $p_0 = 2.5$. The density and horizontal velocity are defined in terms of exponential transition layers of thickness $L = 0.025$, while a small vertical velocity perturbation is imposed to trigger the instability.

The initial conditions are given by:

$$p(x,y) = p_0,$$

$$\rho(x,y) = \begin{cases} \rho_1 - \frac{\rho_1 - \rho_2}{2} \exp\left(\frac{y - 0.25}{L}\right), & y < 0.25, \\ \rho_2 + \frac{\rho_1 - \rho_2}{2} \exp\left(\frac{0.25 - y}{L}\right), & 0.25 \leq y < 0.5, \\ \rho_2 + \frac{\rho_1 - \rho_2}{2} \exp\left(\frac{y - 0.75}{L}\right), & 0.5 \leq y < 0.75, \\ \rho_1 - \frac{\rho_1 - \rho_2}{2} \exp\left(\frac{0.75 - y}{L}\right), & y \geq 0.75, \end{cases}$$

$$u_x(x,y) = \begin{cases} u_1 - \frac{u_1-u_2}{2} \exp\left(\frac{y-0.25}{L}\right), & y < 0.25, \\ u_2 + \frac{u_1-u_2}{2} \exp\left(\frac{0.25-y}{L}\right), & 0.25 \le y < 0.5, \\ u_2 + \frac{u_1-u_2}{2} \exp\left(\frac{y-0.75}{L}\right), & 0.5 \le y < 0.75, \\ u_1 - \frac{u_1-u_2}{2} \exp\left(\frac{0.75-y}{L}\right), & y \ge 0.75, \end{cases}$$

$$u_y(x,y,0) = \varepsilon \, \sin(4\pi x), \qquad \varepsilon = 10^{-2},$$
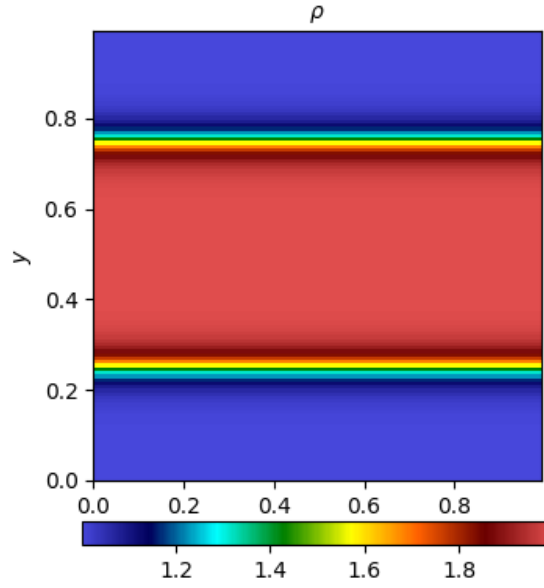
Where $(\rho_1, \rho_2) = (1, 2)$ and $(u_1, u_2) = (+0.5, -0.5)$

Figure 8: Initial Density for $M = 1$ at $t = 0$

We carry out simulations of the Kelvin–Helmholtz instability for various Mach numbers, using a uniform 128×128 grid and a final time $t = 2$ to capture the characteristic roll-up of turbulence.

The results obtained using both Energy and Pressure approach are shown in Figure 9 10. The characteristic roll-up of turbulence is clearly visible, and the flow structures remain stable and well-defined even at low Mach numbers.

(a) $M = 1$

(b) $M = 10^{-1}$

(c) $M = 10^{-2}$

(d) $M = 10^{-3}$
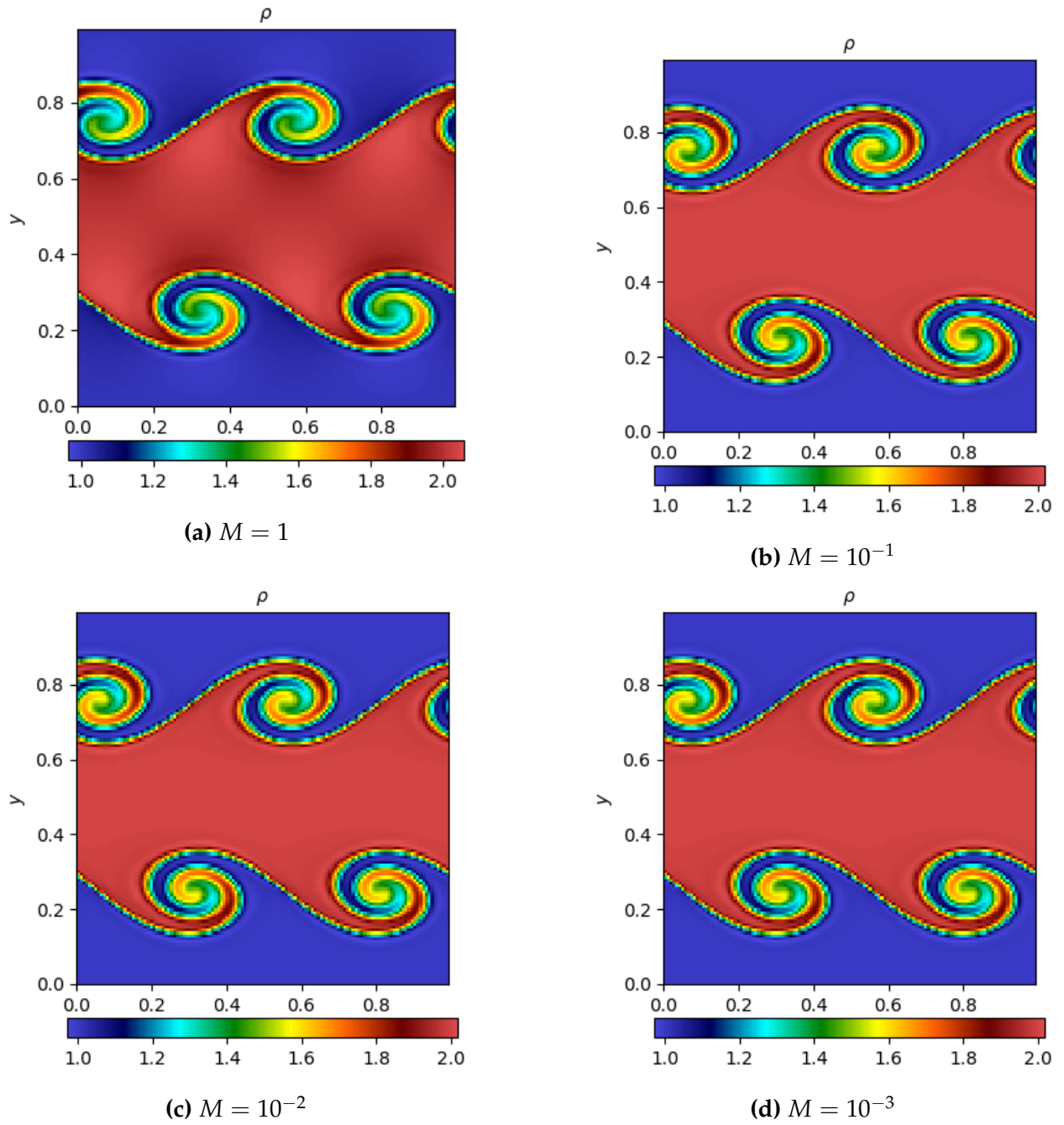
Figure 9: Density for different Mach numbers at $t = 2$ using Energy-based apprach

(a) $M = 10^1$

(b) $M = 10^{-1}$

(c) $M = 10^{-2}$
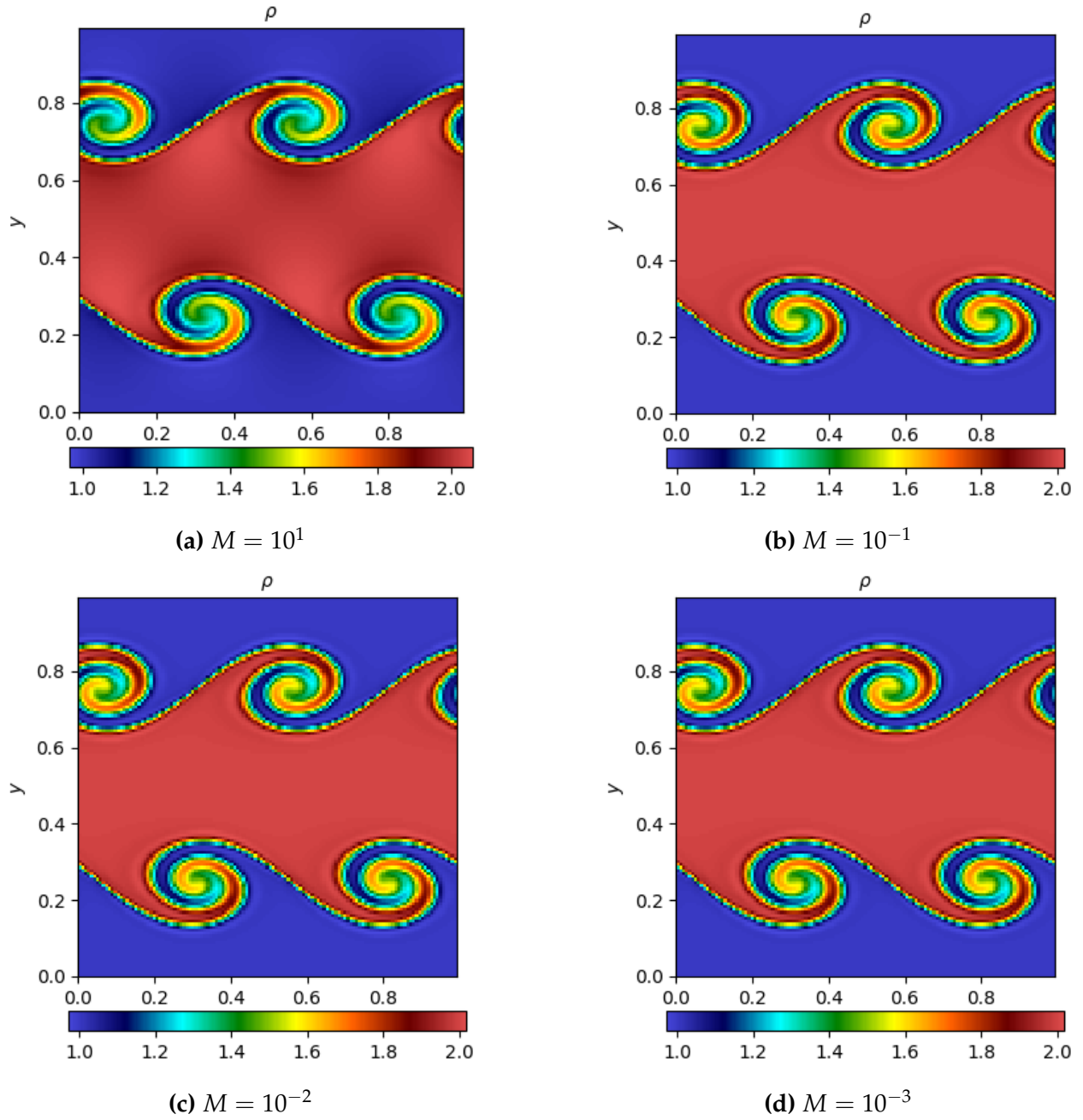

(d) $M = 10^{-3}$

Figure 10: Density for different Mach numbers at $t = 2$ using Pressure-based apprach

5.4   Instabilities

5.4.1   Rayleigh-Taylor

This test case, following the setup of [9, 10], is designed to assess the ability of the numerical scheme to capture interface instabilities under the action of gravity. It considers a radial gravitational field and introduces a small perturbation on a density interface that is initially in isothermal hydrostatic equilibrium. The aim is to trigger and study the evolution of

Rayleigh–Taylor type instabilities in a controlled setting. The gravitational potential is given by:

$$\phi(r) = r,$$

So that gravity points towards the origin. The computational domain is $D = [-1,1] \times [-1,1]$.

The pressure and density are prescribed as:

$$p(r) = \begin{cases} \exp(-r), & r \le r_0, \\ \exp\left(-\frac{r}{\mu} + r_0\frac{1-\mu}{\mu}\right), & r > r_0, \end{cases} \qquad \rho(r,\theta) = \begin{cases} \exp(-r), & r \le r_i(\theta), \\ \frac{1}{\mu}\exp\left(-\frac{r}{\mu} + r_0\frac{1-\mu}{\mu}\right), & r > r_i(\theta), \end{cases}$$

Where the perturbed interface is defined by:

$$r_i(\theta) = r_0\big(1 + \nu\cos(k\theta)\big),$$

And the parameter μ ensures pressure continuity across the interface:

$$\mu = \frac{\exp(-r_0)}{\exp(-r_0) + \Delta\rho}.$$

Parameters $r_0 = 0.5$, a density jump $\Delta\rho = 0.1$, a perturbation amplitude $\nu = 0.02$, Mach number $M = 1$, and wavenumber $k = 20$. The mesh consists of 240×240 Cartesian cells.
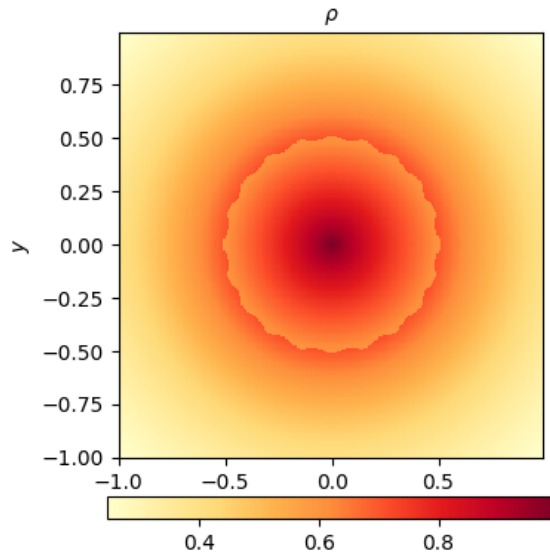

Figure 11: Density perturbation at $t = 0$

From the results shown in Figures 12 and 13, it can be observed that in both formulations the instabilities develop only around the perturbed interface, in agreement with the expected physical behavior. As the computation advances, the perturbations grow and amplify, while the overall hydrostatic balance is preserved. Both the Energy- and Pressure-based formulations successfully capture the correct qualitative dynamics of the instability.
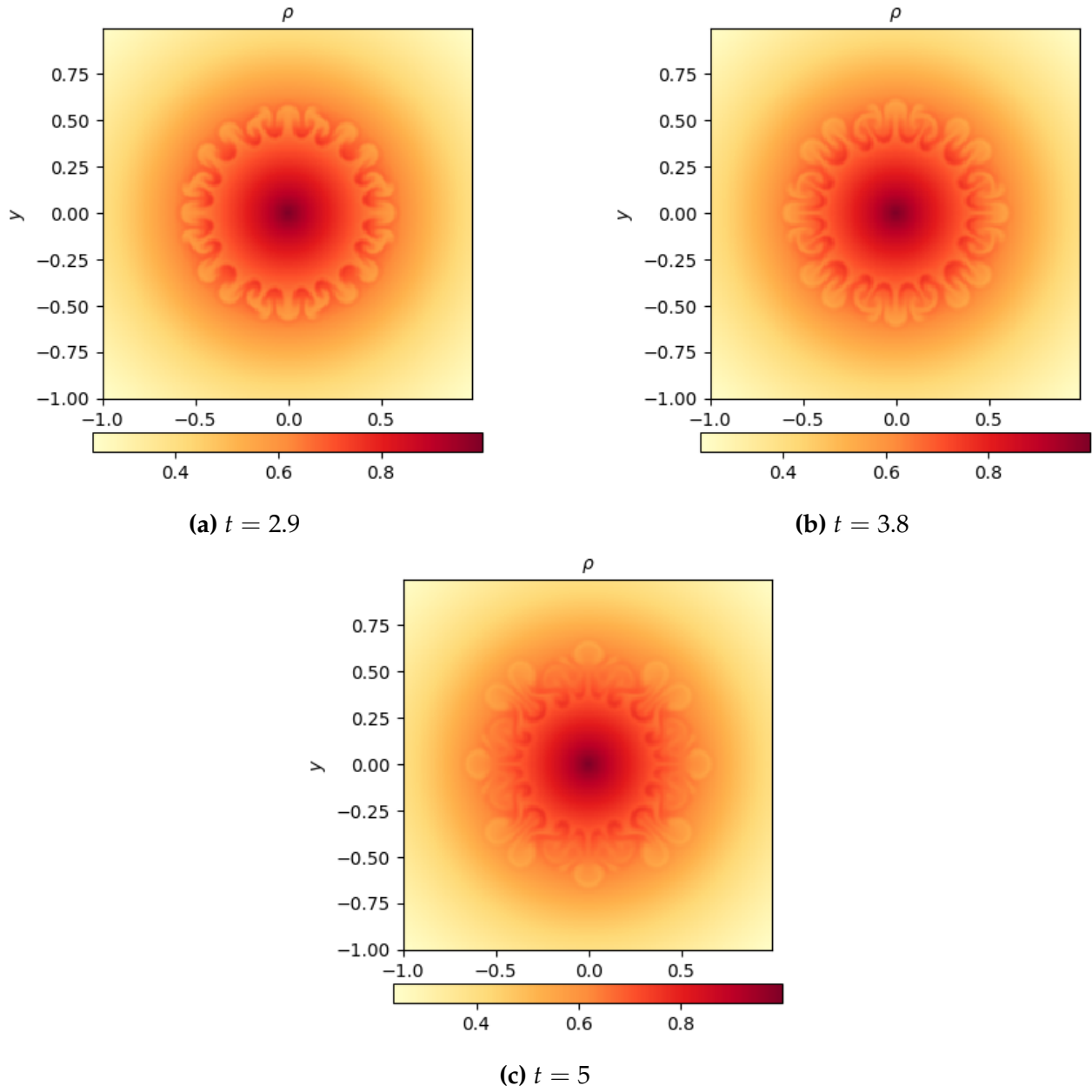
(a) $t = 2.9$

(b) $t = 3.8$

(c) $t = 5$

Figure 12: Rayleigh-Taylor instability in density in radial gravitational field at different times using Energy-based apprach

(a) $t = 2.9$

(b) $t = 3.8$
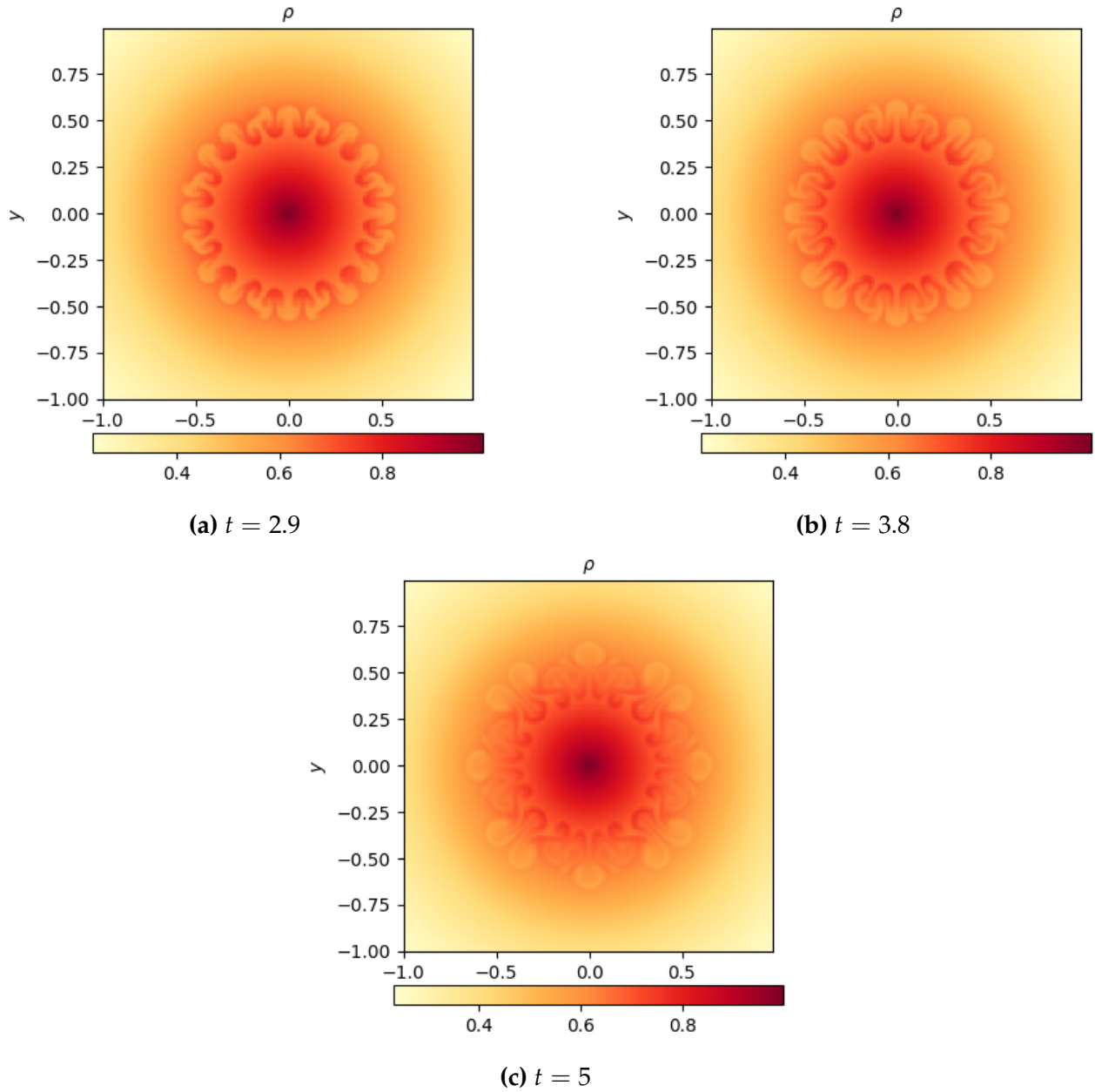

(c) $t = 5$

Figure 13: Rayleigh-Taylor instability in density in radial gravitational field at different times using Pressure-based apprach

5.4.2   Rising bubble

This test case is taken from [4] and describes a warm bubble rising in a stably stratified atmosphere. The computational domain is $D = [0, 10] \, \text{km} \times [0, 15] \, \text{km}$, with gravity acting in the y–direction, given by the gravitational potential:

$$\phi(x, y) = gy, \qquad g = 9.81 \, \text{m/s}^2.$$

The stratification is expressed in terms of the potential temperature:

$$\theta = T \left(\frac{p_0}{p}\right)^{R/c_p},$$

Where c_p is the specific heat at constant pressure, $R = c_p - c_v$ the gas constant, and $p_0 = 10^5$ Pa a reference pressure at sea level. Pressure, density and potential temperature are related through:

$$p = p_0 \left(\frac{\theta R}{p_0}\right)^\gamma \rho^\gamma.$$

Hence, the background atmosphere corresponds to an isentropic state with $\theta = 300\,\text{K}$ and $p(x,0) = p_0$. The hydrostatic equilibrium is given by

$$\nabla p = -\rho \nabla \phi.$$

Which yield a reference Mach number $M = 10^{-2}$ and Froude number $Fr = M$.

The bubble is modeled as a local perturbation in the potential temperature:

$$\delta\theta(x,y) = \begin{cases} \theta_0 \cos^2\left(\frac{\pi r}{2}\right), & r \leq 1, \\ 0, & r > 1, \end{cases} \qquad r = \sqrt{\left(\frac{x-x_c}{r_0}\right)^2 + \left(\frac{y-y_c}{r_0}\right)^2}.$$

The perturbation is centered at $(x_c, y_c) = (5, 2.75)\,\text{km}$ with radius $r_0 = 2.0\,\text{km}$ and amplitude $\theta_0 = 6.6\,\text{K}$. The corresponding perturbation in the pressure is computed consistently from the equation of state.

To transform the data into non-dimensional quantities we use This reference values:

$$x_r = 10^4\,\text{m}, \quad t_r = 10^4\,\text{s}, \quad u_r = 1\,\text{m/s}, \quad \rho_r = 1\,\text{kg/m}^3,$$

the scaling of the physical quantities as summarized in Table **??**:

Quantity	SI unit	Scaling	
x	$[m]$	x_r	
t	$[s]$	t_r	
ρ	$\left[\frac{kg}{m^3}\right]$	ρ_r	
u, c	$\left[\frac{m}{s}\right]$	$u_r = \frac{x_r}{t_r},$	$M = \frac{u_r}{c_r}$
p	$\left[\frac{kg}{m\,s^2}\right]$	$p_r = R_s \rho_r \theta_r,$	$p_r = \rho_r c_r^2$
c_r^2	$\left[\frac{m^2}{s^2}\right]$	$c_r^2 = u_r^2 Fr^{-2}$	
R_s	$\left[\frac{m^2}{s^2 K}\right]$	—	
T, θ	$[K]$	$\theta_r = \frac{u_r^2}{R_s M^2}$	

Table 6: units and scaling relations of the physical quantities

Parameters $\gamma = 1.4$, $R_s = 287.058\,\text{m}^2/(\text{s}^2\text{K})$. The grid consists of 120×180 uniform cells with exact boundary.
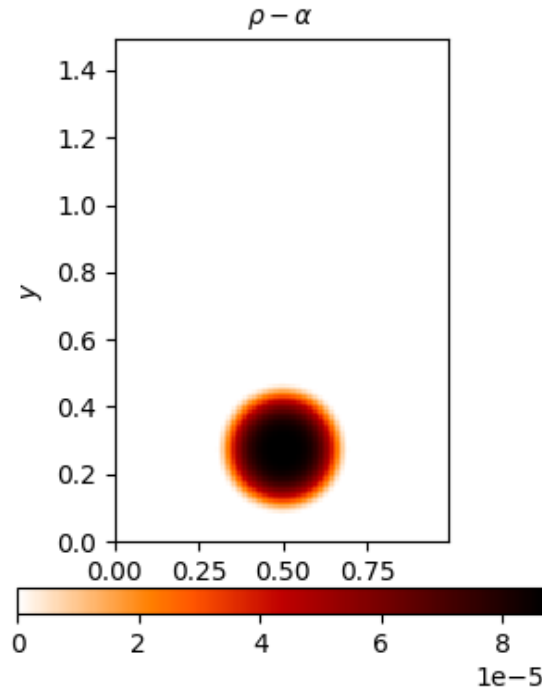
Figure 14: Initial density perturbation at $t = 0$

From the results displayed in Figures 15-16, we observe that the initial warm bubble rises due to buoyancy and progressively deforms as it interacts with the stably stratified background. At $t = 2$ the bubble maintains a coherent structure, while at later times ($t = 3, 4, 6$) the perturbation stretches vertically and instabilities begin to develop along the bubble's boundary. The scheme captures the upward motion and the associated deformation of the bubble without introducing spurious oscillations, which highlights the robustness of Both formulation in this challenging low-Mach and stratified flow configuration.
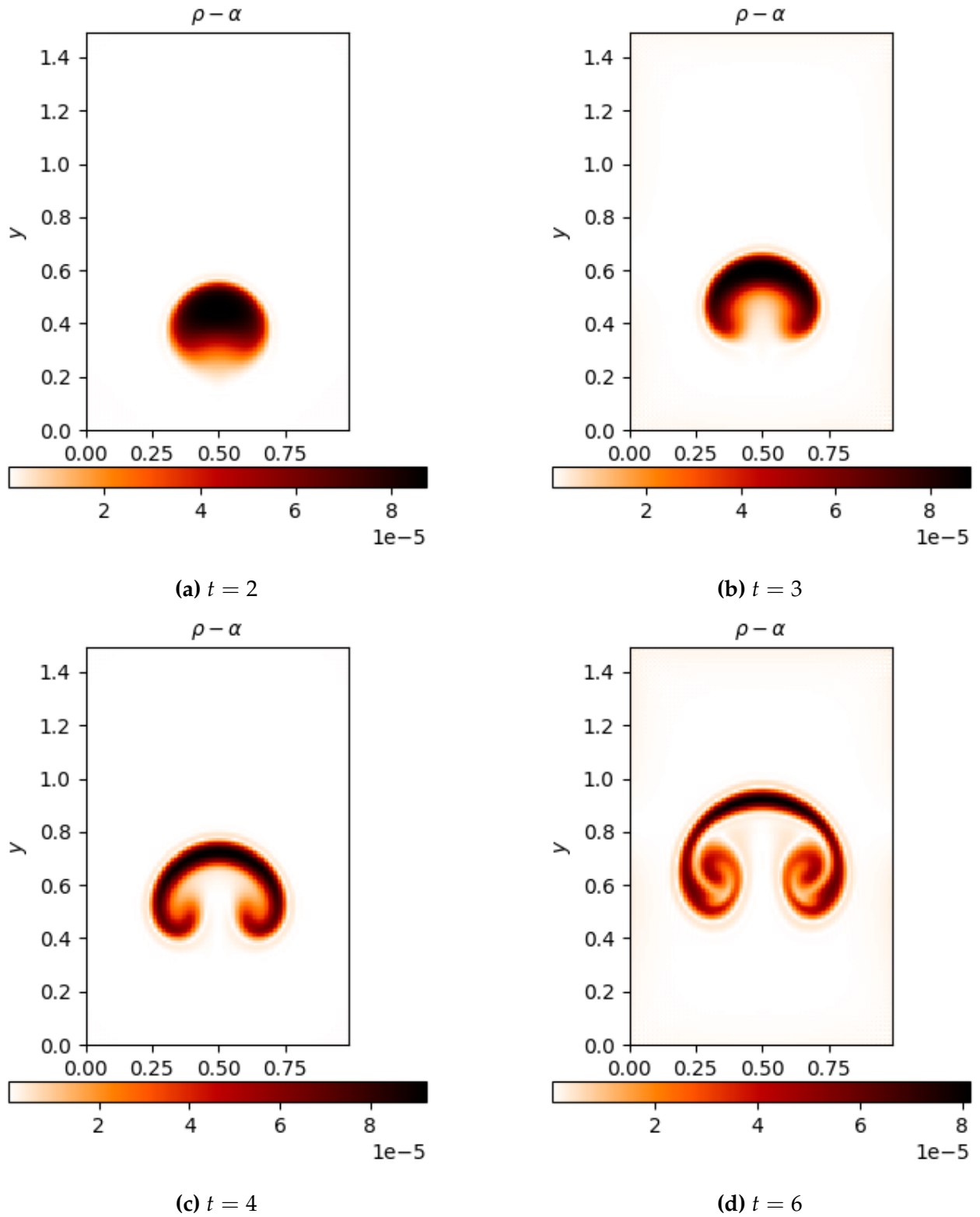
(a) $t = 2$

(b) $t = 3$

(c) $t = 4$

(d) $t = 6$

Figure 15: Density perturbation from the rising bubble using Energy-based apprach

(a) $t = 2$ **(b)** $t = 3$

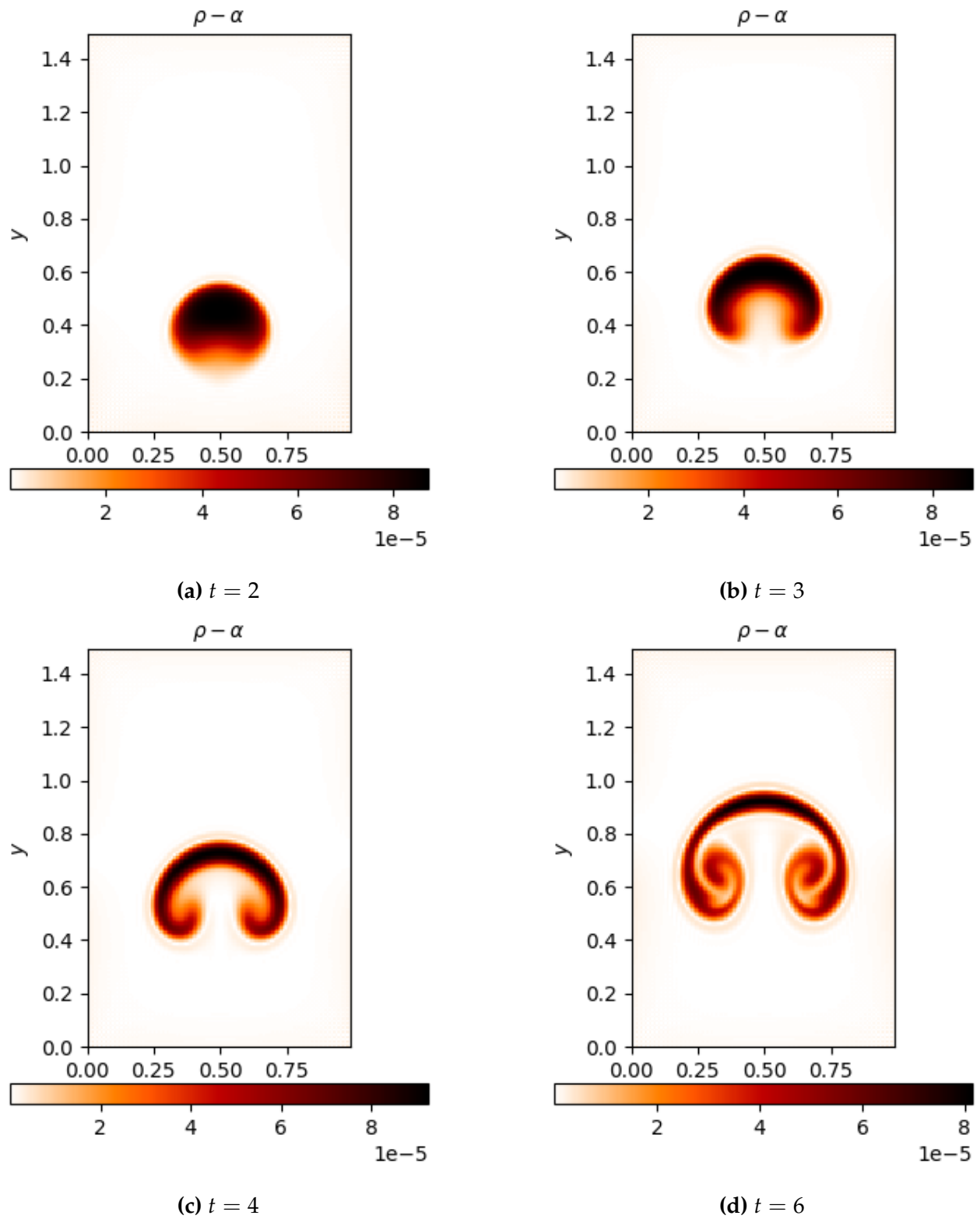**(c)** $t = 4$ **(d)** $t = 6$

Figure 16: Density perturbation from the rising bubble using Energy-based apprach

5.4.3   Bubble shock interaction

This benchmark is inspired by the work of Quirk and Karni [11] on the dynamics of shock–bubble interactions. It models the deformation of a light bubble when impacted

by a planar shock wave. Such configurations are of practical importance in astrophysics, combustion, and high–speed multiphase flows, where density inhomogeneities interact with strong shocks.

We consider a two-dimensional domain $D = [0, 2] \times [0, 1]$ consisting of a background gas with a circular bubble of lower density placed inside. The fluid obeys the Euler equations with ideal gas equation of state, using a fixed adiabatic index:

$$\gamma = 1.4.$$

The background state is at rest with constant pressure:

$$u = v = 0, \quad p = 1.0,$$

and density:

$$\rho = \begin{cases} \rho_{\text{bubble}} = 0.138, & \text{inside the bubble,} \\ \rho_R = 1.0, & \text{right state.} \\ \rho_L = 1.3764, & \text{left state.} \end{cases}$$
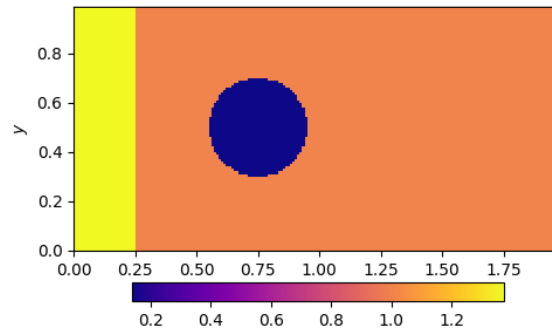
Corresponding to a shock Mach number:

$$M = 1.22.$$

Figure 17: Density at $t = 0$

Figures 18–19 depict the interaction of a shock wave with a light bubble. As anticipated, the impact generates interface roll-up, progressive deformation, and eventual fragmentation of the bubble—hallmark features of this benchmark problem [11]. The simulations confirm that both the Energy- and Pressure-based formulations successfully reproduce the qualitative dynamics of the instability, accurately capturing the bubble's entrainment and pronounced distortion in the post-shock flow.
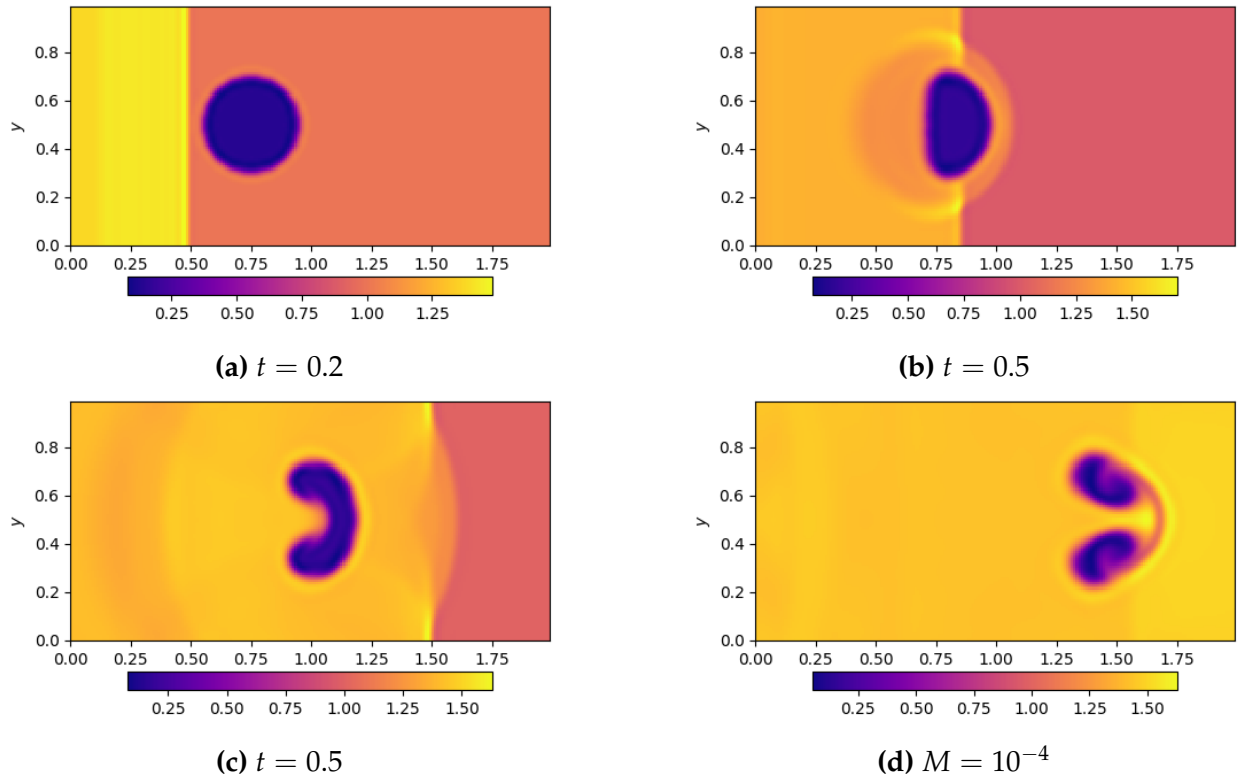
Figure 18: Density at different time using Energy-based approach
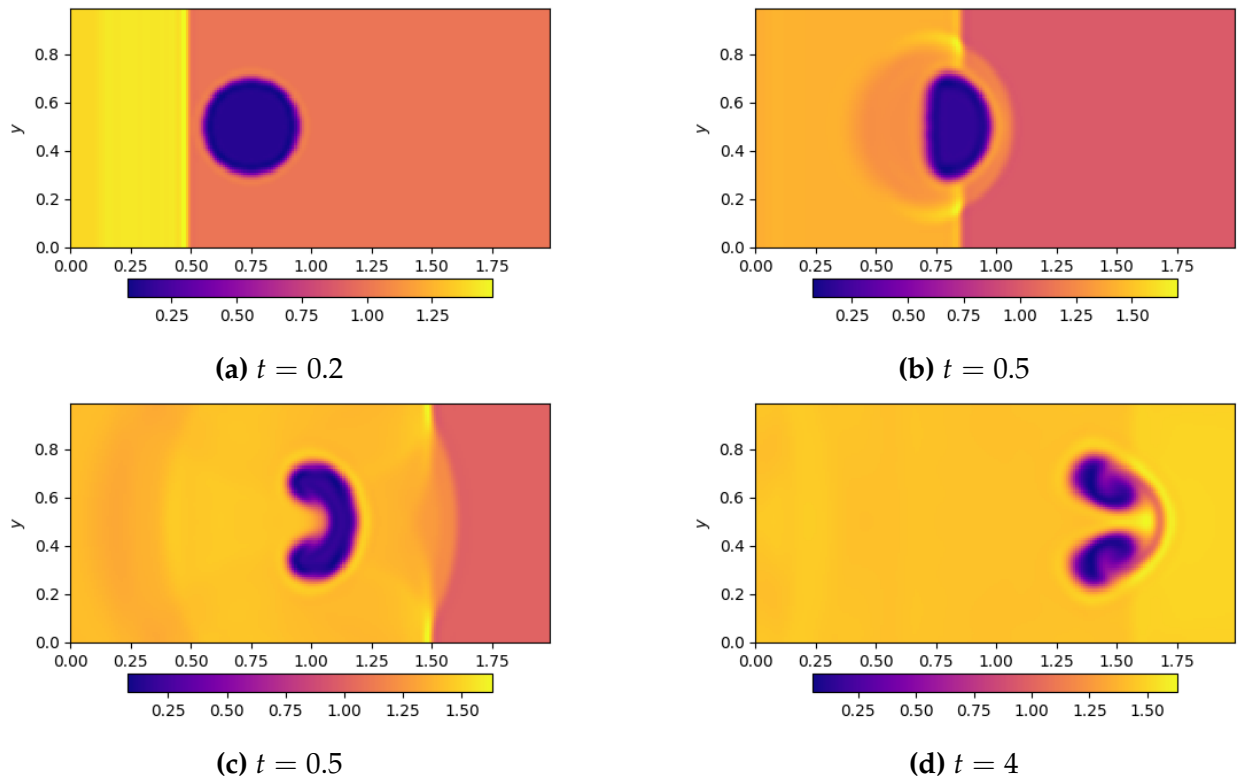

Figure 19: Density at different time using Pressure-based approach

6   Conclusion

In this work, we have developed and analyzed semi-implicit well-balanced schemes for the Euler equations with gravity, with particular emphasis on their performance in the low-Mach regime. The primary objective was to design and evaluate formulations that remain stable, accurate, and robust over a wide range of Mach numbers, while exactly preserving hydrostatic equilibria.

Through a series of benchmark problems—including the Kelvin–Helmholtz instability, the Rayleigh–Taylor instability, the rising bubble, and the shock–bubble interaction, we demonstrated that both the Energy-based and Pressure-based formulations reproduce the expected physical dynamics and capture the essential qualitative features of each test case. At the same time, we observed that the Pressure-based formulation can encounter stability difficulties under specific conditions.

Several challenges emerged during this study. Ensuring stability at very low Mach numbers was particularly demanding, especially for long-time integrations where spurious oscillations and instabilities are prone to develop. Despite these difficulties, the proposed approaches proved effective and allowed us to validate the scheme across a variety of challenging scenarios.

Looking ahead, several directions appear promising. A natural extension of this work would be to increase the accuracy of the scheme to fourth order, as well as to explore more advanced applications relevant to geophysical and astrophysical flows.

Overall, this work has provided both methodological advances and practical insights into the design of robust well-balanced schemes for compressible flows with gravity. It also offered valuable experience in fluid dynamics research, which I intend to pursue further in future studies.

References

[1] Leonhard Euler. Principia motus fluidorum. *Novi Commentarii Academiae Scientiarum Petropolitanae*, 6:271–311, 1761. URL: `https://gidropraktikum.narod.ru/euler1756-1757-eng.pdf`.

[2] Randall J. LeVeque. *Finite Volume Methods for Hyperbolic Problems*, volume 31. Cambridge University Press, Cambridge, 2002. `doi:10.1017/CBO9780511791253`.

[3] Eleuterio F. Toro. *Riemann Solvers and Numerical Methods for Fluid Dynamics: A Practical Introduction*. Springer, Berlin, Heidelberg, 3 edition, 2009. `doi:10.1007/978-3-662-03490-3`.

[4] Andrea Thomann, Gabriella Puppo, and Christian Klingenberg. An all-speed second order well-balanced imex relaxation scheme for the euler equations with gravity. *Journal of Computational Physics*, 420:109723, 2020. `doi:10.1016/j.jcp.2020.109723`.

[5] Sebastiano Boscarino, Giovanni Russo, and Leonardo Scandurra. All mach number second order semi-implicit scheme for the euler equations of gas dynamics. *Journal of Scientific Computing*, 77(2):850–884, 2018. `doi:10.1007/s10915-018-0731-9`.

[6] Uri M. Ascher, Steven J. Ruuth, and Raymond J. Spiteri. Implicit-explicit runge–kutta methods for time-dependent partial differential equations. *Applied Numerical Mathematics*, 25(2-3):151–167, 1997. `doi:10.1016/S0168-9274(97)00056-1`.

[7] Gary A. Sod. A survey of several finite difference methods for systems of nonlinear hyperbolic conservation laws. *Journal of Computational Physics*, 27(1):1–31, 1978. `doi:10.1016/0021-9991(78)90023-2`.

[8] Colin P. McNally, Wladimir Lyra, and Jean-Claude Passy. A well-posed kelvin–helmholtz instability test and comparison. *The Astrophysical Journal Supplement Series*, 201(2):18, 2012. `doi:10.1088/0067-0049/201/2/18`.

[9] Andrea Thomann, Markus Zenk, and Christian Klingenberg. A second-order positivity-preserving well-balanced finite volume scheme for euler equations with gravity for arbitrary hydrostatic equilibria. *International Journal for Numerical Methods in Fluids*, 89(11):465–482, 2019. `doi:10.1002/fld.4703`.

[10] Randall J. LeVeque and Derek S. Bale. Wave propagation methods for conservation laws with source terms. In *Hyperbolic Problems: Theory, Numerics, Applications. Seventh International Conference in Zürich, February 1998, Volume II*, pages 609–618, Basel, 1999. Birkhäuser. `doi:10.1007/978-3-0348-8724-3_12`.

[11] James J. Quirk and Smadar Karni. On the dynamics of a shock–bubble interaction. *Journal of Fluid Mechanics*, 318:129–163, 1996. `doi:10.1017/S0022112096007069`.